EFFECTIVE METHODS TO REDUCE THE RF-INDUCED HEATING FOR MEDICAL IMPLANTS IN MRI

by
Rui Yang

A dissertation submitted to the Department of Electrical and Computer Engineering,
Cullen College
in partial fulfillment of the requirements for the degree of

Doctor of Philosophy

in Electrical and Computer Engineering

Chair of Committee: Ji Chen

Committee Member: David R. Jackson

Committee Member: Jiefu Chen

Committee Member: Driss Benhaddou

Committee Member: Wolfgang Kainz

University of Houston
May 2020

ACKNOWLEDGMENTS

Pursuing a doctoral degree is harder than I thought but more rewarding than I could have ever imagined. It would have been impossible without my academic advisor, Dr. Ji Chen. He guided and encouraged me at every stage of the research. He taught me to be professional and do the right thing even when the road got tough.

I am eternally grateful to the members of my dissertation committee: Dr. David Jackson, Dr. Jiefu Chen, Dr. Driss Benhaddou and Dr. Wolfgang Kainz. They provided me with constructive criticism and valuable advice. Their knowledge and insights have greatly enriched my research work.

I would also like to thank the past and current colleagues in my research laboratory: Dr. Jianfeng Zheng, Dr. Qingyan Wang, Dr. Dawei Li, Dr. Xin Huang, Dr. Xinyu Liu, Dr. Qi Zeng, Dr. Jingshen Liu, Dr. Ran Guo, Dr. Xiaohe Ji, Mr. Zhichao Wang, and Mr. Yu Wang for their persistent assistance, support, and encouragement. Discussing research and problems with them benefits me a lot. I enjoy the days working with them.

Finally, I want to say thank you to my parents: Qiyong Yang and Yaping Bai. You are always the people that I could turn to during my dark and desperate days. You make me feel confident whenever I doubt myself. Without your support and encouragement, I would have stopped and given up a long time ago. It is great to have your back in my life.

ABSTRACT

Radiofrequency (RF) –induced heating is one of the primary safety concerns for patients with medical implants undergoing magnetic resonance imaging (MRI). Due to this potential hazard, patients with medical devices are usually contraindicated from the MRI process. With the steady growth in the number of patients with medical implants that require MRI, it is important to address the issue of RF heating in MRI. This dissertation focuses on techniques and methods to reduce the RF-induced heating so that patients with medical implants can undergo MRI safely.

For the implantable leads, it was proposed to modify the electrode structure to reduce the RF-induced heating. We show that enlarging the electrode contact reduces the rate of RF energy deposition at the electrode, which results in less RF-induced heating at the lead tip.

For the external fixation devices, the strategy of using capacitive structures has been investigated to reduce the RF-induced heating. Both simulations and experiments demonstrated that introducing proper capacitive structures to the external fixation device could reduce the temperature rise by more than 95% at both 1.5 T and 3 T. An equivalent circuit was developed to illustrate the heating reduction effect of the capacitive structures in the external fixation device. It is concluded from the circuit model that increasing the equivalent impedance of the external fixation device reduces the RF-induced heating.

For the passive implants, we investigated the effects of two different incident RF fields generated by a transverse electromagnetic (TEM) coil and a birdcage (BC) coil on the RF-induced heating. Electromagnetic simulation results show that the BC coil generates a stronger incident electric field along the coil bore than the TEM coil does.

Due to this reason, orthopedic plates and spinal fixations caused a higher RF heating in the BC coil than they did in the TEM coil. For passive implants with large dimensions along the coil bore, the TEM coil provides a greater safety margin for patients while the BC coil provides a more conservative heating evaluation.

TABLE OF CONTENTS

LIST OF TABLES

LIST OF FIGURES

Chapter 1

Introduction

Magnetic resonance imaging (MRI) has become a routine imaging method used in hospitals and clinics for medical diagnosis over recent decades. Compared with computed tomography (CT) which is better suited for imaging hard structures like bones, MRI provides better contrast and higher resolution in visualizing soft tissues such as the brain, spine, joint, and muscle. Moreover, unlike CT where X-ray beams are sent through the human body, the main techniques used in MRI are a powerful magnetic field and radio frequency (RF) pulses. Therefore, MRI does not have ionizing radiation and long-term health risks. Although MRI is regarded as one of the safest imaging methods in clinics, patients with medical devices are usually contraindicated from MRI due to the potential safety hazards including the undesired force, torque, tissue heating, image artifacts, and device malfunction [1]. Most of these concerns can be avoided by using non-magnetic material for medical implants, however, the RF field used during the MRI process can still cause a severe heating effect to the human tissue. This RF-induced heating is well known and has been investigated by numerous studies.

In this chapter, we first introduce the RF-induced heating caused by different metallic medical devices, including the orthopedic device, artery stent, external fixation, and active implantable lead. Next, we review the existing standards and guidelines for evaluating the RF-induced heating of medical implants. Last, we present the motivation and objective of this dissertation.

1.1 RF-induced Heating Issue

During the MRI process, the human body is exposed to a strong RF field generated by the RF coil. The RF field can penetrate the human body and interact with the human tissue, ultimately resulting in the heating effect. In the presence of metallic medical implants, this heating effect can become extremely severe and even cause thermal damage to the surrounding tissue. As patients with medical implants sometimes need to be placed under the MRI machine for detailed musculoskeletal examinations, there arises a safety concern regarding the RF-induced heating of the implants. In this section, we review previous studies that focused on the RF-induced heating of different medical implants.

1.1.1 Passive Implant

The passive implant is an implant that serves its function without the supply of electrical power. A typical example is the orthopedic medical device, which is widely used to treat damaged bone problems. Typically, orthopedic implants consist of pins, rods, plates, screws, nails, stems, and prostheses. They can be applied to different human bone places as shown in Figure 1-1.

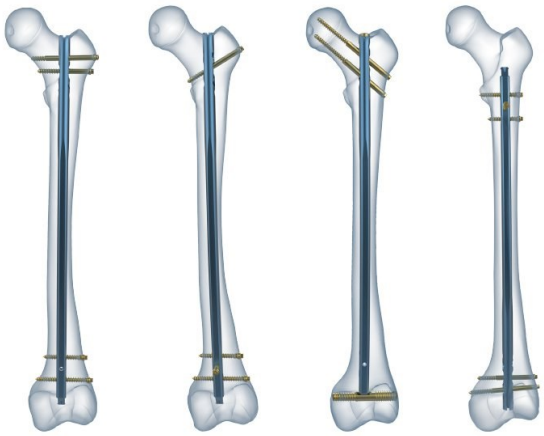

Figure 1-1. Examples of the orthopedic medical device.

The RF-induced heating of orthopedic implants is highly dependent on the dimension and structure of the implanted device. For example, Liu et al. numerically investigated the RF-induced heating of the bone plate system and found that the maximum heating of the device is almost linearly proportional to the dimension of the orthopedic implant when it is less than 100 mm for both 1.5 T and 3 T MRI [2]. As the length of the device varies from 21 mm to 107 mm, the maximum energy deposition increases from 15.8 W/kg to 91.5 W/kg at 1.5 T and from 8.6 W/kg to 42.5 W/kg at 3 T. When the dimension of the device is greater than 100 mm, the linear relation does not exist for 3 T MRI. Zheng et al. investigated the RF-induced heating for multi-component orthopedic hip replacement systems [3]. They showed that the stem and screw lengths were the most important factors influencing the RF-induced heating for both field strengths. In addition to the dimension of the implants, the position of the coil relative to the body also affects the heating effect significantly. It was shown that the RF heating would be insubstantial if the prostheses were located outside the coil [4]. However, when the prostheses were within the coil, the local specific absorption rate (SAR) near the device would exceed the recommended limits in the normal mode.

Another example of passive implants is the medical stent. As shown in Figure 1-2, a stent is a metal tube inserted into the lumen of an anatomic vessel to keep the passageway open. There are a wide variety of stents used for different purposes, such as coronary stents, vascular stents, and biliary stents. The relationship between the design parameters and the RF-induced heating of the stent has been widely investigated.

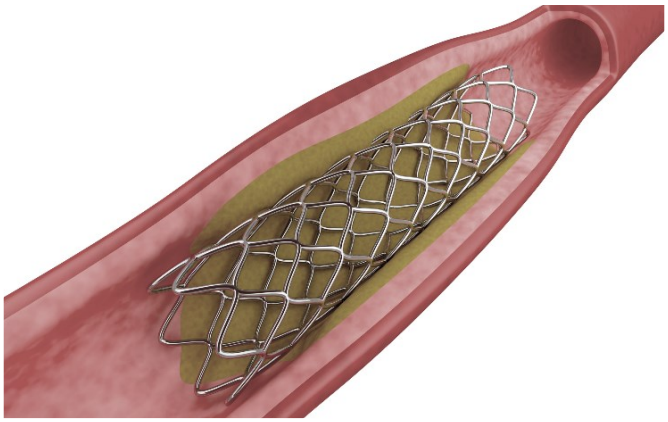

Figure 1-2. A stent used to open the vascular blocked by the fat.

Lukas et al. showed that the length and the orientation of the coronary stent could influence RF heating significantly [5]. An increase in the stent length induced a rise in RF heating. Besides, the RF heating would be maximum as the long axis of the stent was parallel with the electrical field. Ji et al. studied the effects of the stent pattern on the RF heating and found that the stent with non-electrically connected segments resulted in lower RF-induced heating compared to the electrically connected pattern [6]. In an experimental study, measurements demonstrated that the segmented design could reduce the temperature rise from 4.52 °C to 1.76 °C under 15-min MRI RF exposure [7]. In addition to the stent pattern, the length, diameter, pitch, and gap of the stent would also affect the RF-induced heating of the stent [8]. It was found that as the stent length is larger than 100 mm, the pitch size increment causes higher RF-induced heating while the gap size increment leads to a reduction of RF-induced heating. Moreover, the pitch variation affects the worst-case length of the stent. A larger pitch tends to lead to a longer worst-case stent length.

The external fixation device is a surgical device used to stabilize bone fractures. A typical external fixation device consists of three parts: (1) metallic pins to be screwed into

the fractured bones, (2) rods or bars made of carbon fiber or metallic materials to bridge the pins, and (3) metallic clamps to connect the pins and the rods. Figure 1-3 shows two common external fixation devices.

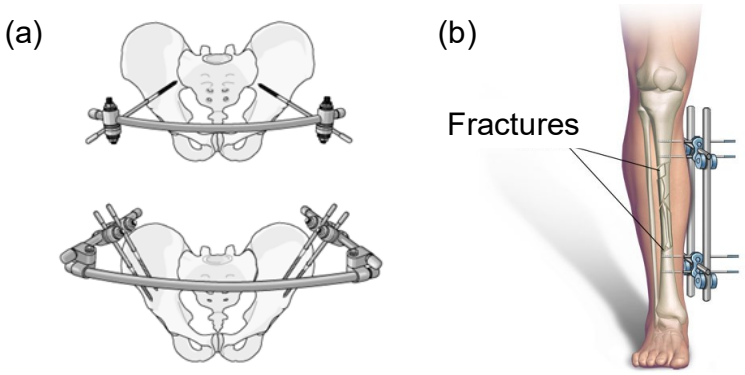

Figure 1-3. (a) Pelvic external fixation and (b) tibia external fixation.

Comparing with other passive implants, the rods and clamps are outside the human body thus are much closer to the RF coils [9]. It was observed that the external fixation device often has higher heating than that of fully implanted passive devices [10], [11]. Y. Liu et al. investigated the RF-induced heating of a generic external fixation device and fully considered the impacts of the dimensions and configurations of the devices on the RF-induced heating [10]. It was shown that the shortest insertion depth and the largest pin spacing with the conductive bar would result in the worst-case heating for modular external fixation devices. With the worst-case configuration, the modular external fixation device can lead to a temperature rise of over 50 °C.

1.1.2 Active Implant

One of the most important RF heating concerns is the RF-induced heating at the tip of active implantable medical devices (AIMD). AIMD is a medical device relying its functioning on a source of electrical energy. Examples of AIMDs include implantable cardiac pacemakers, neurostimulator systems, and cochlear implants.

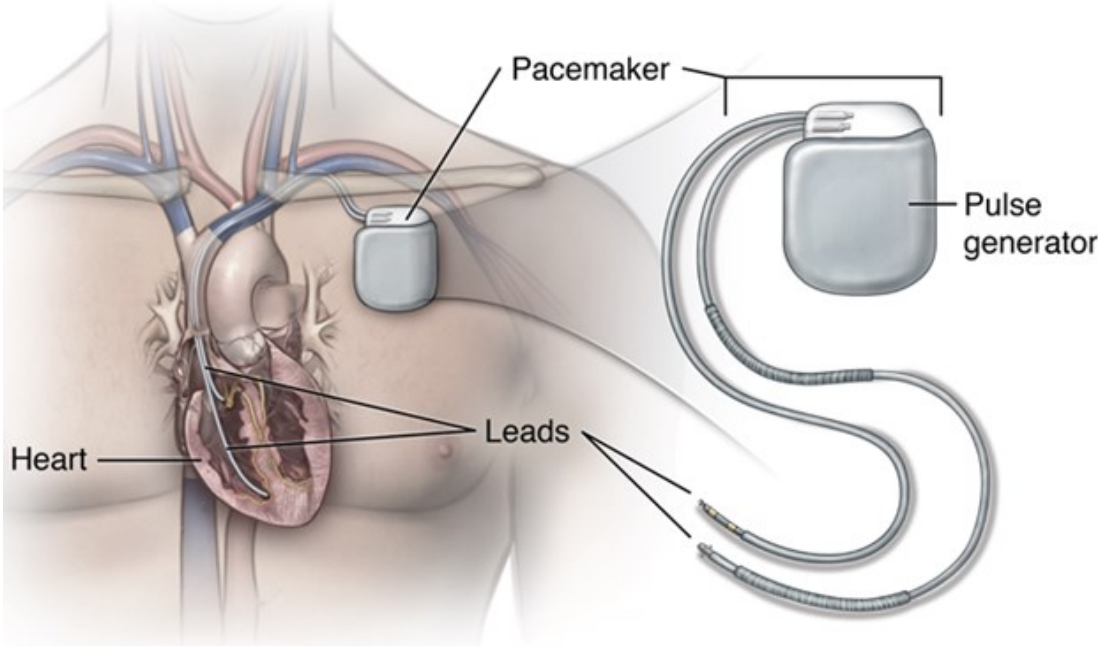

Figure 1-4. A cardiac pacemaker in the human body.

Generally, an AIMD consists of three parts: (1) the implantable pulse generator, (2) the insulated lead, and (3) the exposed electrode at the distal lead end, as shown in Figure 1-4. Since the elongated lead of AIMD is insulated along the lead body, RF energy received by the AIMD lead will be delivered and concentrated at the lead tip. This would potentially cause severe thermal damage to the tissue at the lead tip. There are several medical accidents reported because of the RF-induced heating effects at the metal lead tip [12], [13]. Figure 1-5 shows some examples of the damages due to the RF heating effects from the AIMDs during the MRI process. Figure 1-5 (1) shows a third-degree skin-burn caused by an MRI-conditional electrocardiographic monitoring system. Figure 1-5 (2) shows the overheated and melted intracranial pressure transducer in the brain and Figure 1-5 (3) shows a cause of a thermal brain injury.

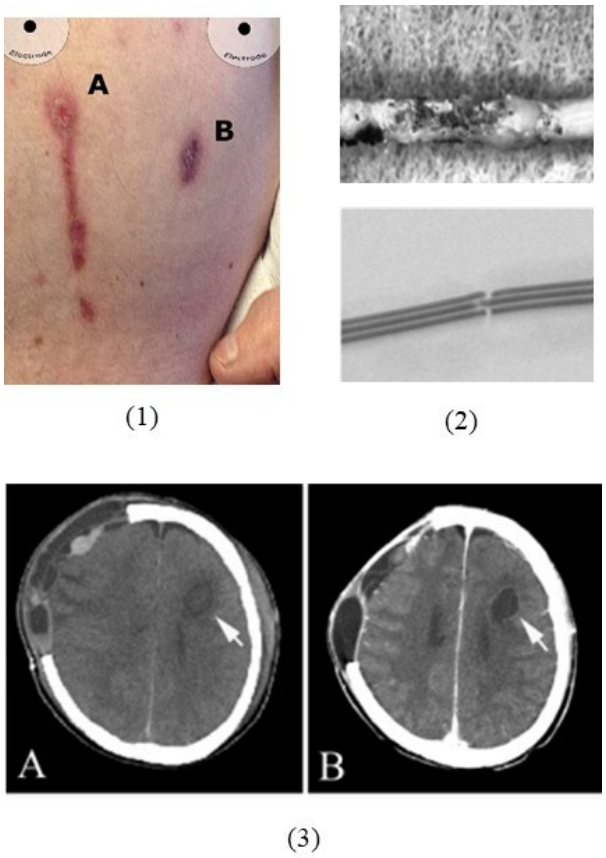

Figure 1-5. Examples of the damages due to RF heating during MRI. (1) shows the skin burn caused by an MRI-conditional metal device. (2) shows the overheated and melted medical device in the brain, and (3) shows the resulting thermal brain injury.

It is well known that the RF-induced heating is caused by the coupling between the long conductors of the AIMD and the RF coil of the MRI scanner. Yeung et al. showed that the magnitude and phase distribution of the electric field affects the RF heating [14]. Also, the insulation thickness, the wire length and the relative permittivity of the insulator have a significant impact on the RF-induced heating [15]. Another effect is the lead trajectory in the patient's body [16], [17]. In addition to the lead properties, it is found that the lead-to-case impedance can significantly influence the induced currents in the implant leads [18], [19]. The transmission line model was proposed to formulate the relationship between the electrode heating and the lead-case impedance [20], [21].

To evaluate the temperature rise near the electrode of an AIMD, Park et al. in 2007 proposed the transfer function method [22]. According to this method, the temperature rise near the electrode can be calculated by integrating the lead transfer function and the tangential incident electric field along the lead trajectory. This method connects the RF-induced heating to the incident field along with the lead, and it is widely used in other studies to analyze the problem and predict the temperature rise [23], [24].

1.2 Heating Regulations and Evaluations

To ensure the safety of patients under MR scanning, the U.S. Food and Drug Administration (FDA), as well as the International Electrotechnical Commission (IEC), have guidelines to state the specific absorption rate (SAR) and temperature limits for the whole body as well as the local level exposure as shown in Table 1-1 [25], [26].

Table 1-1. FDA and IEC guidelines for SAR and temperature limits during an MRI scan

Limit		Whole-Body Average	Heat Average	Head, Trunk Local SAR	Extremities Local
FDA		4 W/kg for 15 minutes	3.2 W/kg for 10 minutes	8 W/kg in 1 g for 10 minutes	12 W/kg in 1 g for 5 minutes
IEC (6-minute average)	Normal (all patients)	2 W/kg (0.5 °C)	3.2 W/kg	10 W/kg	20 W/kg
	First level (supervised)	4 W/kg (1 °C)	3.2 W/kg	10 W/kg	20 W/kg
	Second level (IRB approval)	> 4 W/kg (> 1 °C)	> 3.2 W/kg	> 10 W/kg	> 20 W/kg
	Localized heating limit	39 °C in 10 g	38 °C in 10 g		40 °C in 10 g

For patients with implanted devices made of metallic materials, a much harsher constraint should be obeyed because of the severe localized RF heating. In 2005, a set of MRI labeling terms for medical devices was developed and released [27]. They are as follows: (1) MR Safe – a medical device that poses no known hazards resulting from exposure to any MR environment. MR Safe medical devices are composed of materials that are electrically nonconductive, nonmetallic, and nonmagnetic. (2) MR Conditional – a medical device with demonstrated safety in the MR environment within defined conditions. At a minimum, the conditions of the static magnetic field, the switched gradient magnetic field, and the RF field should be addressed. Additional conditionals, including specific configurations of the medical device, may be warranted. (3) MR unsafe – a medical device that poses unacceptable risks to the patients, medical staff, or other personas within the MR environment.

When assessing the safety of a medical device within the MR environment or developing MRI safety information for the medical device labeling, following FDA-recognized standards and guidance can be used.

The standard F2182-11a covers the measurement of RF-induced heating on or near a passive medical implant and its surroundings during MRI [28]. According to the standard, the implant to be tested is placed in a phantom material that simulates the electrical and thermal properties of the human body. The implant is placed at a location with well-characterized exposure conditions. An RF field producing a sufficient whole-body averaged SAR of about 2 W/kg averaged over the volume of the phantom is applied for approximately 15 min.

The standard ISO/TS 10974 covers the safety assessment of the AIMD in patients who undergo a 1.5 T MRI [29]. Determining the temperature rise in local tissue due to the interaction of an AIMD with the RF field of an MRI scanner is a complicated process. It depends on AIMD design, MRI scanner technology (RF coil and pulse sequence design), patient size, anatomy, position, AIMD location, and tissue properties. Depending on the specific conditions, the variation of in-vivo temperatures may span several orders of magnitude. In the standard ISO/TS 10974, a four-tier testing approach is described to accommodate the diversity of AIMD configurations and specific applications. After the determination of a conservative estimate of energy deposition, including the uncertainty, in a controlled in-vitro system, the second step is to assess the maximum in-vivo temperature rise using previously assessed energy deposition.

1.3 Motivation

MRI has become a popular medical imaging technique over recent decades owing to its noninvasive nature and high-resolution image quality for soft tissues [30], [31]. However, patients with medical implants are usually contraindicated from MRI, because of the concerns for harmful interactions between MRI fields and the implanted device. There are many accident reports regarding injuries of patients with medical implants during MRI examinations. One of the major safety hazards during MRI for patients with medical implants is RF-induced heating. As the number of patients with medical implants requiring MRI is rapidly growing, the issue of RF-induced heating needs to be addressed. The objective of this dissertation is to develop effective and safe methods to reduce the RF-induced heating of medical implants so that such patients can undergo the MRI process safely.

In this dissertation, three novel methods are proposed to reduce the RF-induced heating associated with the AIMDs, external fixations, and passive implants. Both numerical simulations and experiments were performed to demonstrate the effectiveness of the methods. Moreover, the underlying mechanism of each method to reduce the heating is investigated and illustrated in this work.

1.4 Outline

The remainder of this dissertation is organized as follows. Chapter 2 introduces the evaluation methods of the RF-induced heating used in this study. Chapter 3 investigates the impacts of the electrode design on the RF-induced heating of an AIMD implanted lead. It is demonstrated that increasing the radial contact of the lead electrode can be an effective method to reduce the heating effect of the AIMD. In Chapter 4, the strategy of using capacitive structures has been investigated to reduce the RF-induced heating of external fixation devices. Both simulations and experiments demonstrated that introducing proper capacitive structures to the external fixation device could reduce the temperature rise at both 1.5 T and 3 T MRI. From the perspective of the circuit model, capacitive structures were applied to the external fixation to decouple the interaction between the device and the RF field. In Chapter 5, we investigated the effects of two different incident RF fields generated by a transverse electromagnetic (TEM) coil and a birdcage (BC) coil on the RF-induced heating. Numerical simulation results show that implants with large dimension along the coil bore cause higher heating in the BC coil than they did in the TEM coil. In Chapter 6, we summarized the main works and conclusions of this dissertation and discuss the future directions for the studies presented in this dissertation.

Chapter 2

Methodology

This chapter describes the basic methodology used in this dissertation. We start with the underlying mechanism of the RF-induced heating, including the overall RF energy absorbed by the human body as well as the more localized and stronger RF-induced heating effect in the presence of implanted medical devices. Next, we introduce the electromagnetic simulation and the thermal simulation used to calculate the RF-induced heating. Last, the experimental setup is presented, including the RF-induced heating assessment system and the transfer function measurement.

2.1 RF-induced Heating Mechanism

During the MRI process, the RF coil of an MRI machine will generate a very strong RF field. While the magnetic field part is essential and lays the foundation of MRI, the electric field part invites troubles [31]. As the RF field penetrates the human body, part of the electromagnetic energy will be absorbed by the human tissues that are conductive, and consequently converted into heat effect and arise thermal temperature rise. To quantify the rate at which RF energy is absorbed by the human body, the specific absorption rate is used and can be calculated as

$$\mathrm{SAR}(r) = \frac{\sigma}{2\rho}\left|\underline{E}^{tot}(r)\right|^2, \tag{1}$$

where σ is the local conductivity of human tissues, ρ is the mass density and $\left|\underline{E}\right|$ is the magnitude of the electric field from the RF coil. The SAR value is usually averaged over a given amount of volume. For example, the amount of RF energy absorbed by the whole

human body is referred to as the whole-body-averaged SAR. Similarly, we have 1-gram spatial-average SAR (SAR_{1g}) which is averaged over a volume with a weight of one gram.

The subsequent heat transfer problem can be model using the tissue bio-heat equation. According to the Pennes bio-heat equation [32], the temperature rise in the human body could be calculated as

$$\rho c \frac{\partial T(r,t)}{\partial t} = \nabla \cdot \left(k \nabla T(r,t)\right) + \rho SAR(r) + q_p + q_m, \tag{2}$$

where ρ is the density of human tissues, c is the specific heat capacity of human tissues, T is the tissue temperature, k is the thermal conductivity, SAR is the specific absorption rate of the tissues, q_p is the blood perfusion, q_m is the metabolic heat generation. Studies performed by Shellock et al. [33], [34] indicates that an MR procedure performed at a whole-body averaged SAR of 6.0 W/kg can be physiologically tolerated by an individual with normal thermoregulatory functions. To date, this is the highest level of RF energy that human subjects have been exposed to in association with MR procedures.

In the presence of the medical implant, the RF field will interact with the metallic parts of the medical implant. During this interaction, a surface current is induced on the surface of the device [7]. The scattered field produced by the induced current can be written as

$$\underline{E}^s(r) = -j\omega\mu \int_S \mathcal{G}(r,r')J(r')ds, \tag{3}$$

where $\mathcal{G}(r,r')$ is the dyadic Green's function, $J(r')$ is the induced surface current. The total electric field contributing to the SAR value in Equation (1) is the summation of the incident field and the scattered field

$$\underline{E}^{tot}(r) = \underline{E}^{i}(r) + \underline{E}^{s}(r). \quad (4)$$

If the observation point is near the implant, the magnitude of the scattered field is much larger than the incident field and the incident field can be neglected in practice. As the observation point moves away from the device, the scattered field decreases rapidly due to the decay of Green's function and the loss of the surrounding medium. In this case, the incident field dominates, and the scattered field can be ignored. This fact indicates that the RF-induced heating of medical implants is a localized effect and the RF-induced heating hot spot is at the vicinity of the implant's tip.

2.2 Numerical Simulation

SEMCAD X, a commercial full-wave electromagnetic field solver based on the finite-difference time-domain (FDTD) method, is used to compute the electric field distributions in this study. The software can build 3D solid modeling for medical devices and solve coupled EM-thermal simulations. Moreover, it provides computable human phantoms with advanced tissue models for directly analyzing the real-world biological phenomena.

2.2.1 MRI RF Coils Modeling

To generate the RF field in the MRI system, two high-pass birdcage coils were built as shown in Figure 2-1. Both coils have a diameter of 63 cm and a height of 65 cm. The eight parallel red lines represent the phased current sources and the sixteen blue lines at end rings are the tuning capacitors. The capacitors were adjusted to make the coil resonant at 64 / 128 MHz, which corresponds to the Larmor frequency of 1.5 / 3 T MRI system. The tuning process can be found in [35]. Quadrature mode was used to excite the RF coil. To generate a circular polarized RF field inside the coil, the magnitude of each

current source is set to be the same and the phase difference between adjacent current sources is 2π/N, where N is the total number of rungs (N = 8 in our case) [36].

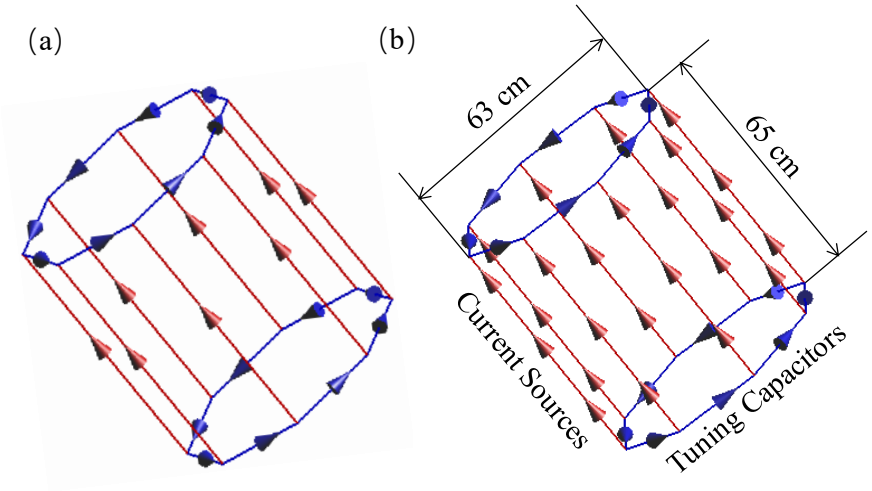

Figure 2-1. Structures of (a) 1.5 T RF body coil, (b) 3 T RF body coil.

Figure 2-2 shows the magnetic field distributions at the center plane of the two RF coils. As we can see from Figure 2-2, the magnetic field is uniformly distributed for both birdcage coils. The good homogeneity of the magnetic field distribution indicates that the two RF coils are operating at the correct resonant mode. This simplified coil will be used for MRI RF heating simulation studies.

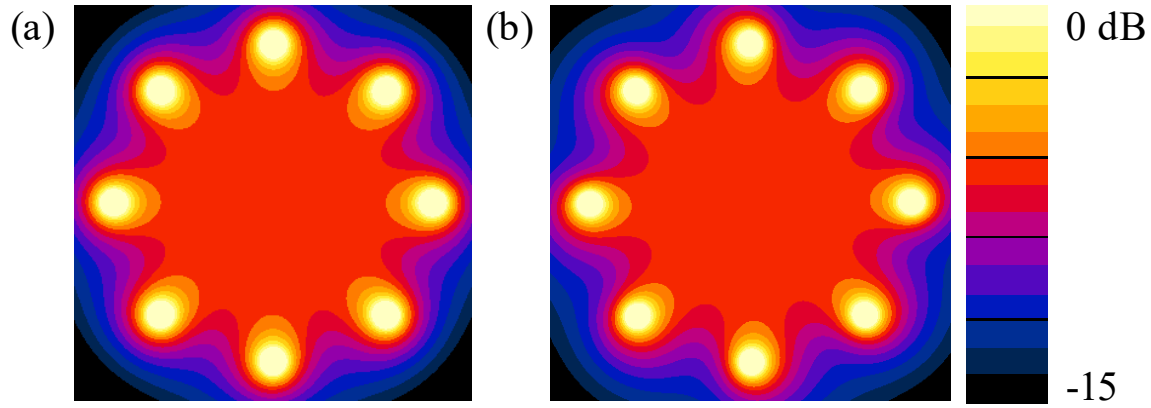

Figure 2-2. Magnitude distribution of magnetic field on the center plane of (a) 1.5 T coil, and (b) 3 T coil. 0 dB corresponds to 1 μT.

2.2.2 ASTM Phantom and Virtual Population

To evaluate the RF-induced heating near the testing medical implants, the American Society for Testing and Material (ASTM) standard F2182-11a suggests that a phantom material that simulates the electrical properties of the human body should be used [28]. According to the standard, the phantom container is made of electrical insulating materials that are non-metallic and non-magnetic. The phantom gel, which simulates the human tissue, has the conductivity of 0.47 S/m and the relative permittivity of 80.4. The trunk part of the phantom is 42 cm wide and 60 cm high. The head part of the phantom is 15 cm wide and 27 cm high. The thickness of the phantom gel is 9 cm. Figure 2-3 shows the overall dimension of the ASTM phantom.

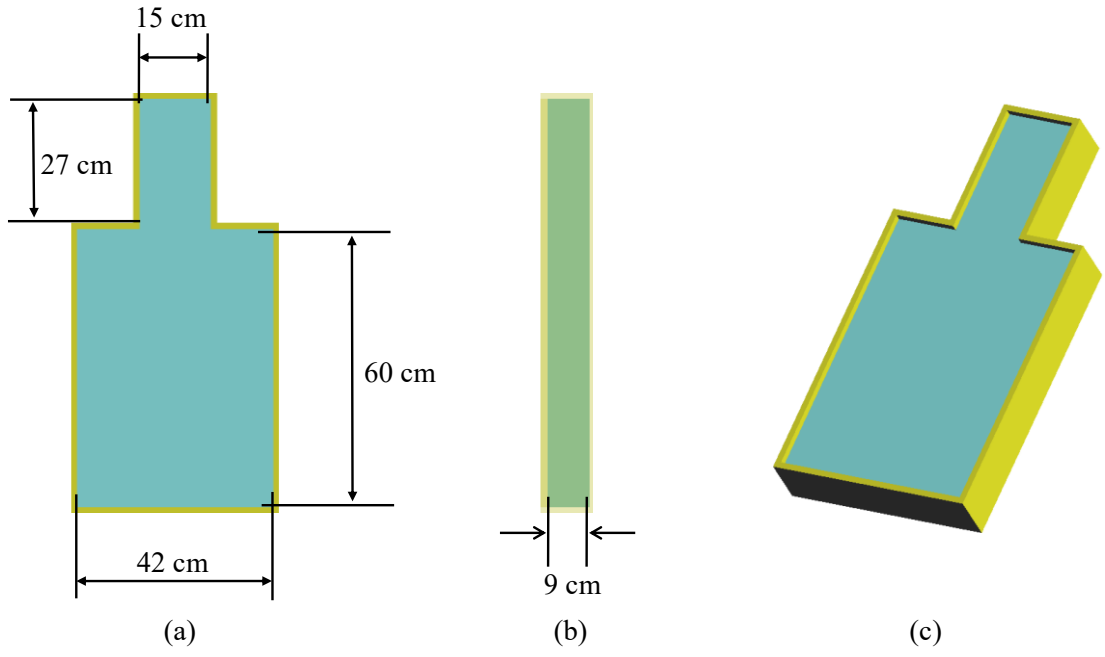

Figure 2-3. (a) The front view, (b) side view, and (c) angle view of the ASTM phantom used in the simulation.

During RF exposure, the ASTM phantom is placed at the center of the RF coil, as shown in Figure 2-4. According to the ASTM standard, the device under testing should

be placed at the location where the electric field is strong, to obtain a conservative RF-induced heating result. Electromagnetic simulations are performed to determine the electric field distribution in ASTM phantom in Figure 2-5, with Figure 2-5 (a) showing the 1.5 T coil result and Figure 2-5 (b) showing the 3 T coil result, respectively. As we can see, the maximum electric field locations are near the vertical sidewall of the phantom for both 1.5 T and 3 T coil. Therefore, in this study, the device is placed at the mid-axial plane about 2 cm away from the vertical sidewall for all simulations.

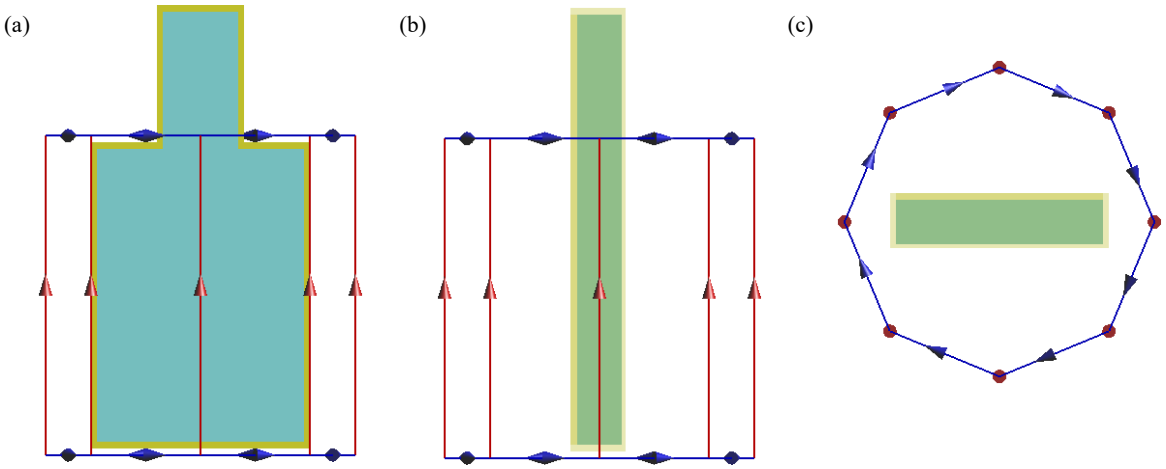

Figure 2-4. (a) The front view, (b) side view, and (c) top view of the ASTM phantom inside a non-physical birdcage coil.

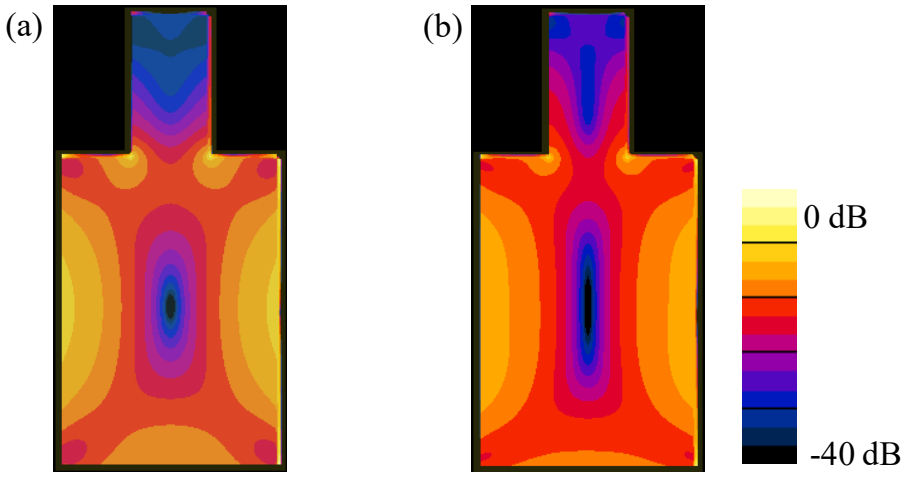

Figure 2-5. Magnitude distribution of electric field on the center plane of (a) 1.5 T coil, and (b) 3 T coil. 0 dB corresponds to 400 V/m.

In addition to the ASTM phantom, the virtual population models were also used for analyzing real biological effects [37], [38]. The virtual population models are a set of detailed high-resolution anatomical models with approximately 80 organs and tissues [37]. The virtual family contains five different human models, including obese male (Fats), adult male (Duke), adult female (Ella), girl (Billie), and boy (Thelonius) as shown in Figure 2-6. The electromagnetic properties of each tissue at 1.5 T and 3 T can be obtained from the ITIS foundation database.

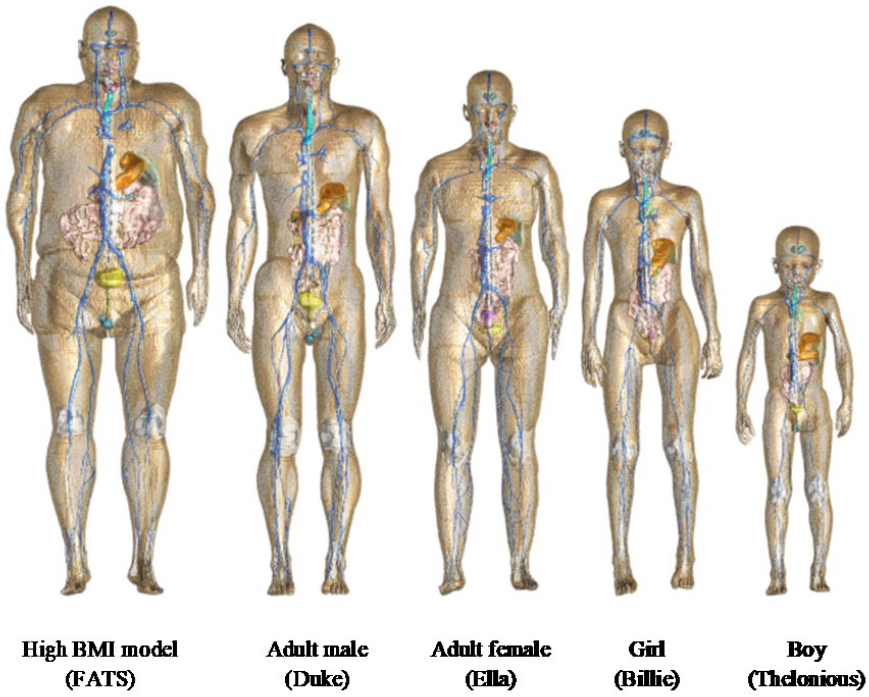

Figure 2-6. The five human models of the virtual family.

2.2.3 Thermal Simulations

Thermal simulations were performed using the thermal solver in the SEMCAD X that solves the Penne bioheat equation described in Equation (2). In the in-vitro study, no metabolic heat or blood perfusion occurs, thus the original heat transfer equation can be simplified as

$$\rho c \frac{\partial T(r,t)}{\partial t} = \nabla \cdot \left(k \nabla T(r,t)\right) + \rho SAR(r), \quad (5)$$

where k, ρ, and c are the thermal conductivity, density, and specific heat capacity of the medium, respectively. Table 2-1 summarized the thermal parameters of the materials used in this study.

Table 2-1. Thermal parameters

Material	Thermal Conductivity (W/m/K)	Specific Heat Capacity (J/kg/K)
Phantom Shell	0.2	1000
Phantom Gel	0.47	4160
Metal	7	400

2.3 Experimental Setup

2.3.1 RF-induced Heating Measurement

During experiments, both 1.5 T and 3 T MRI RF coils were used for validation. To simulate the RF field in 1.5 T MR Scanner, Zurich MedTech (ZMT) Medical Implant Test System (MITS) is used. The entire system locates in a standard shielded room (by ETS-Lindgren). MITS birdcage is protected with an internal shield. The RF coil of the MITS 1.5 system is using a high-pass birdcage coil with a 650 mm length operating at 64 MHz. The birdcage shield has a length of 850 mm, with a 700 mm inner diameter plastic shell and an 850 mm outer diameter metal shield. By adjusting the initial input parameters on the MITS 1.5 system, a circular polarization RF electromagnetic field can be obtained inside the RF coil, which is nearly the same as numerical simulation.

To perform the temperature measurements, we built an ASTM phantom followed the standard F2182-11a. The ASTM phantom was filled with gelled saline, which was made of sodium chloride (NaCl, 1.32 g/L) and polyacrylic acid (10 g/L) dissolved in water, to achieve a conductivity of 0.47 S/m at room temperature. The depth of the gelled

saline is 90 mm. To obtain the maximum temperature rise during the RF exposure, we placed the optical-fiber thermal probes at the tips of the device. The total exposure time of the tested device in the RF field is 12 minutes at 1.5 T and 6 minutes at 3 T. The experimental setup used in this study is shown in Figure 2-7.

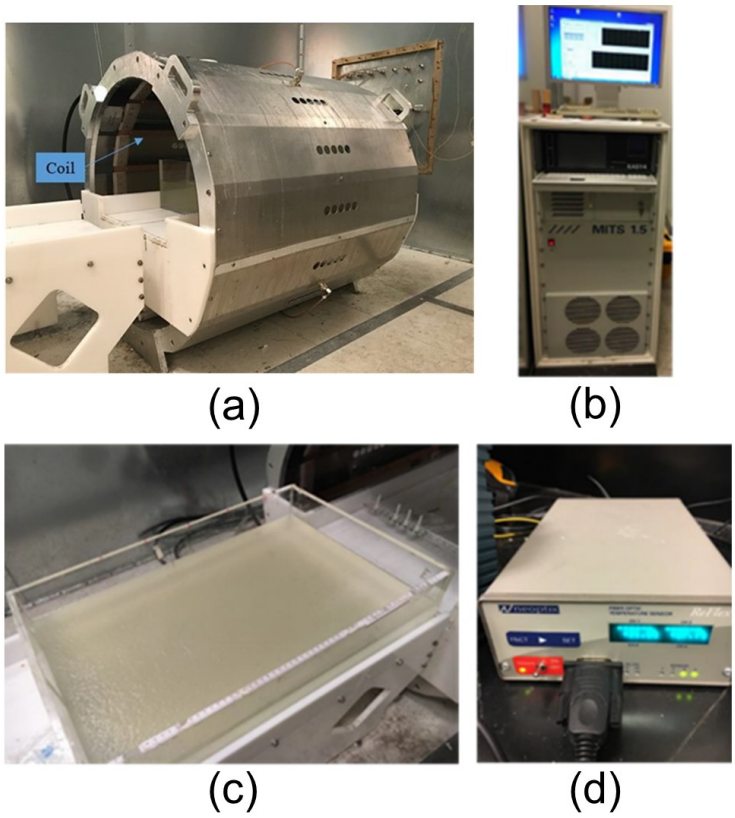

Figure 2-7. The RF-induced heating assessment system including (a) a 1.5 T MRI RF coil, (b) the operating console, (c) the ASTM rectangular phantom and (d) four-channel fiber optic temperature sensors.

2.3.2 Transfer Function Measurement

According to the reciprocity theorem [23], the lead transfer function relates the incident tangential electric field along the lead body to the induced electric field near the electrode as shown below

$$|E_{tip}| = \left| \int T_L(l') \cdot E_{L,inc}(l') dl' \right|, \quad (6)$$

where $T_L(l')$ is the current distribution along the lead body when applying a unit current source at the lead electrode, $E_{L,inc}(l')$ is the incident tangential electric field along the lead trajectory inside the phantom without the implanted device in place, and E_{tip} is the induced electric field near the electrode. The transfer function of the lead can be used to estimate the heating near the electrode.

$T_L(l')$ of the lead can be measured using the setup shown in Figure 2-8. The lead is placed vertically in the center of the phantom gel. The S_{21} parameter can be measured with port 1 of vector network analyzer (VNA) connected to the electrode and port 2 connected to a current probe placed at location l'. The measured S_{21} value along the lead body is the unscaled transfer function in amplitude and phase. For simple lead wire, the transfer function can also be obtained using numerical simulation [23]. In the numerical approach, the lead is immersed in a lossy medium having the same electric properties as the gel. A small electric dipole source is then placed at the electrode as the excitation. The current distribution along the lead body is then calculated using $\oint H \cdot dl = I$ on an arbitrary closed loop around the lead cross section. The calculated current distribution is the lead transfer function.

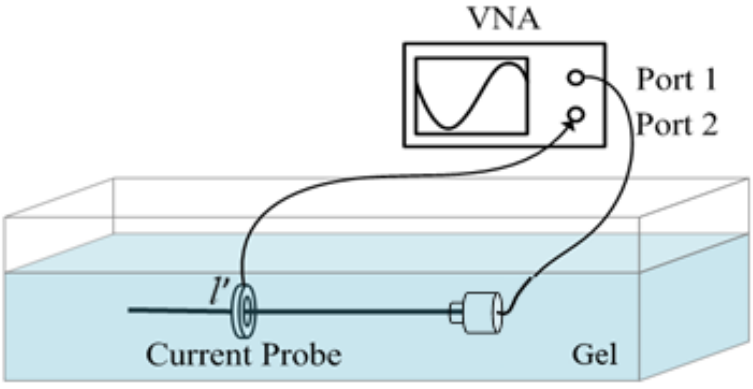

Figure 2-8. The transfer function measurement setup.

Chapter 3

Reducing RF-induced Heating for an AIMD Implanted Lead through Novel Electrode Design

3.1 Background

The RF-induced heating issue associated with AIMDs during the MRI process is well known. To reduce such risk associated with AIMDs, many mitigating techniques have been studied. One method is to introduce a resonant structure near the lead tip to prevent the RF energy from propagating to the electrode [39]. This resonant coil acts as a band stop filter which only prevents the energy propagation to the exposed lead tip but allows the therapy signals of a different frequency to be delivered to the target nerves. However, this coil configuration can only provide a maximum reduction at a particular frequency. Moreover, extremely high heating can occur near the coil itself. Later, Rupam and Hyoungsuk showed that adding pins along the lead body, which increases the contacting area between the lead and the human tissues, could effectively reduce the deposited RF energy at the electrode, subsequently mitigating the heating effect [40]. Although this unique lead design can reduce the heating level at various MRI RF frequencies, the complex mechanical structure increases the difficulty of manufacturing and reduces the long-term reliability of the lead.

In addition to improving the lead design of AIMD, recent works have shown that pads made of high dielectric material (HDM) can reduce the RF-induced heating for pacemaker [41], [42]. The HDM can reduce the RF power level required for imaging while maintaining the strength of the RF magnetic field. However, the HDM designs are

often MRI-system-specific and patient-specific, and it is challenging to manufacture an HDM pad with relative permittivity up to about 500. The most straightforward way to solve the RF-induced heating and RF-induced malfunction for the AIMD is to build a panel to shield the RF field. In 2005, a thin, one-layer patch was employed to absorb RF energy [43]. Then, innovatively, M. S. Sarto et al. built a multilayer absorbing panel for RF fields with high transparency in the visible range [44], [45]. The thickness and number of layers have significant influences on the performance of the absorbing shields [46]. Most designs of the absorbing RF energy shields, panels, or wearable clothes are aimed to cover the human torso, arm, or leg [47].

While most studies focus on the lead body of the AIMD, rare attention has been paid to the structure of the lead electrode. In this paper, the impact of the electrode structure on the RF-induced heating is investigated. Both simulations and experiments are performed.

3.2 Cuff Electrode Design

Nerve cuff electrodes such as the vagus nerve stimulator, are designed for reliable recording and stimulating peripheral nerves [48]. A cuff electrode is generally fabricated using metallic foil [49]. As shown in Figure 3-1, the foil is encapsulated in silicone elastomer and a window is cut on the contact surface to create an interface with the nerve.

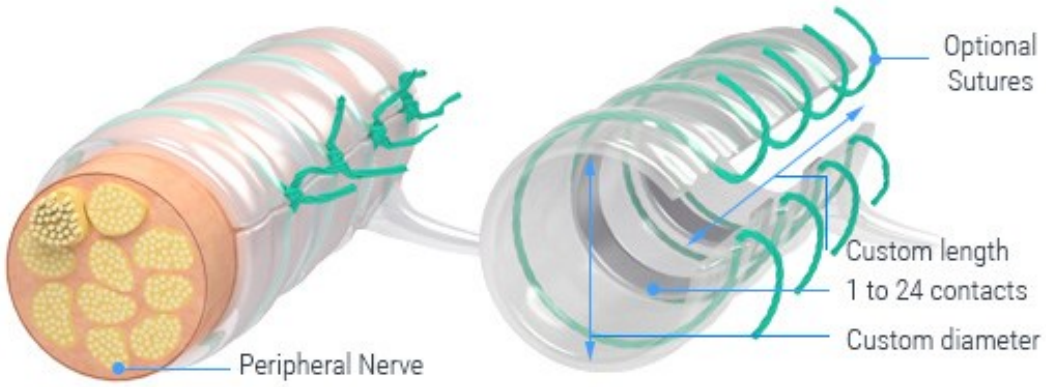

Figure 3-1. Example of a nerve cuff electrode.

To investigate the impact of the electrode on the RF-induced heating of an AIMD lead, three different sizes of cuff electrodes were evaluated in this study. As shown in Figure 3-2, they are a 90º radial contact electrode (0.25 circle), a 180º radial contact electrode (0.50 circle), and a 270º radial contact electrode (0.75 circle). Each cuff electrode is modeled as a perfect electric conductor (PEC) and has an inner radius of 1.2 mm, an outer radius of 1.5 mm, and a length of 1.5 mm. The silicone elastomer surrounding the foil is modeled using the insulating material with a relative permittivity of 2 and a thickness of 0.5 mm. Each cuff electrode is connected to a PEC wire with a diameter of 0.4 mm. The length of the wire is varied from 150 mm to 250 mm. Both electromagnetic simulations and thermal simulations were performed to assess the RF-induced heating of the electrodes in SEMCAD X 14.8.

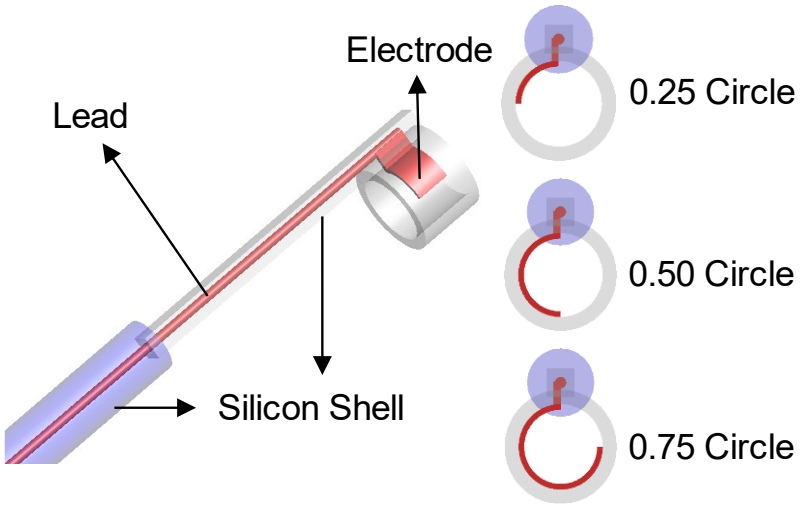

Figure 3-2. Model of a generic nerve stimulator and three different structures of cuff electrode.

3.3 RF-induced Heating Evaluation

The effects of the electrode size were investigated for different lead lengths. Figure 3-3 and Figure 3-4 show the variations of the peak local SAR_{1g} and temperature rise with electrode size for different lead lengths, respectively. From Figure 3-3, increasing the lead length or increasing the radial contact of the electrode will increase the peak local SAR_{1g}. By comparison, it is found from Figure 3-4 that the temperature rise increases with the lead length while decreases with the electrode size, which is inconsistent with the local SAR result. For example, as the radial contact of the electrode increases from 90° to 270°, the peak SAR_{1g} is increased from 296.69 W/kg to 364.06 W/kg while the temperature rise is reduced from 45.4 °C to 38.8 °C. This finding indicates that for a cuff electrode with larger radial contact, more RF energy received by the lead is delivered to the distal electrode. However, this increment in RF energy does not convert to a worse heating effect. Instead, the heating effect is mitigated by the large electrode.

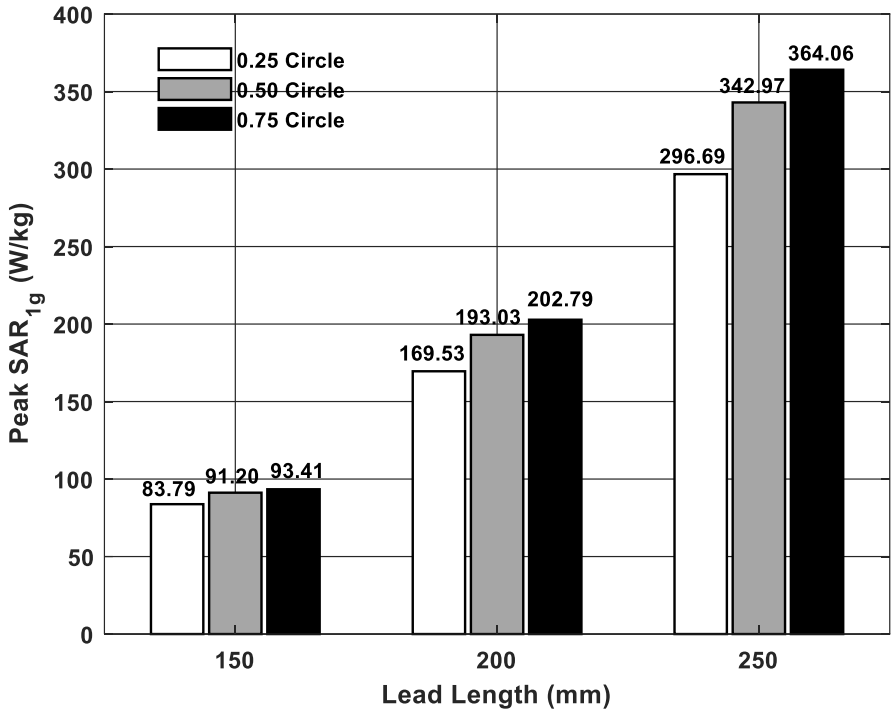

Figure 3-3. Peak SAR_{1g} values at the electrodes for different lead lengths and electrode sizes.

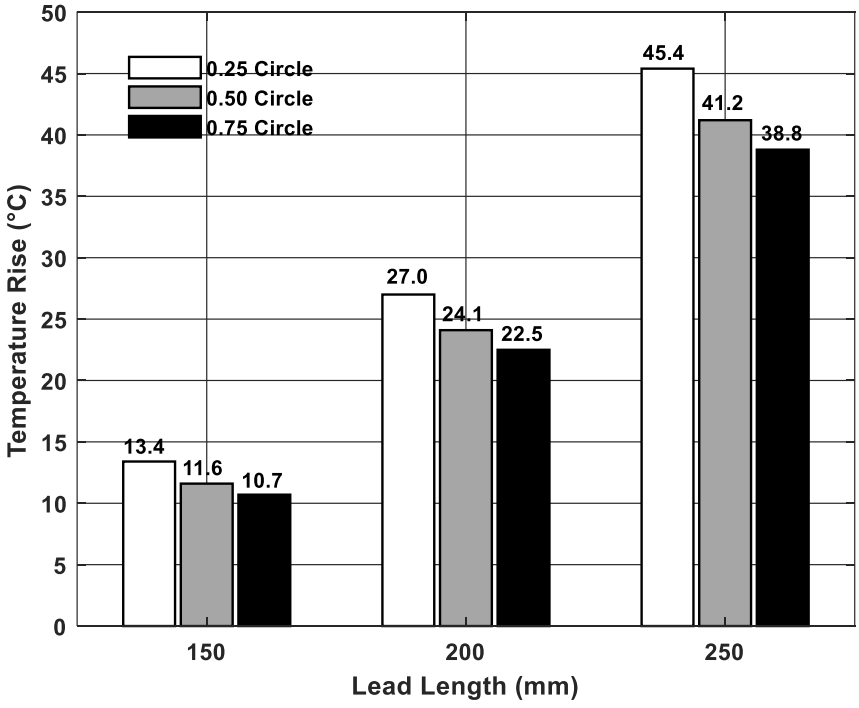

Figure 3-4. Temperature rises at the electrodes for different lead lengths and electrode sizes.

To understand the reason why a larger radial-contact electrode can reduce the RF-induced heating, the distributions of non-averaged SAR were calculated and plotted in Figure 3-5. As we can see, the RF energy is primarily deposited at the interface between the foil and the phantom. For the same cuff electrode, the magnitude of the non-averaged SAR increases with the lead length, while the pattern keeps unchanged. Therefore, as a larger RF energy is deposited at the electrode, the temperature rise will increase for the same radial contact.

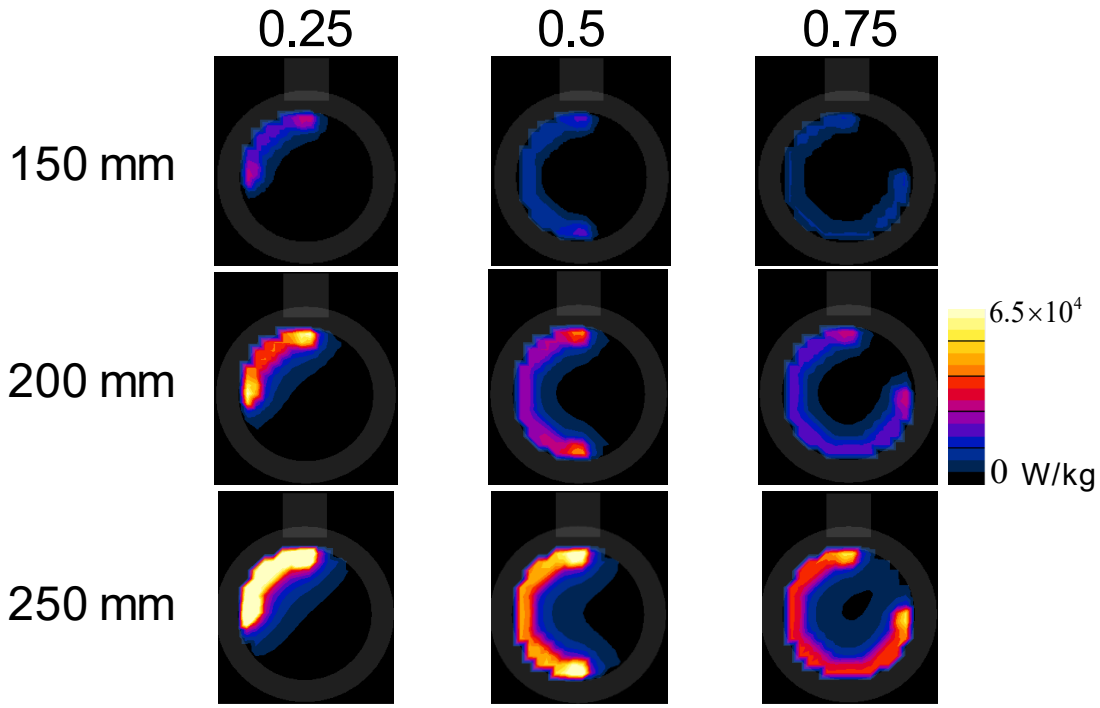

Figure 3-5. Non-averaged SAR distributions at the electrodes of the leads with different lengths.

However, as the radial contact of the electrode increases, the energy deposition density at the electrode is decreased. Even though the total energy deposited at the electrode is increased, the reduced energy deposition density mitigates the RF-induced heating for a larger radial contact electrode.

The peak local SAR1g values and temperature rises at different electrodes are summarized in Table 3-1. It is concluded that the local SAR_{1g} or the deposited RF power at the electrode cannot correctly reflect the heating level for the medical implant with fine structure, such as lead electrodes. This is because, in addition to the localized RF energy at the electrode, the SAR distribution also has a significant effect on the RF-induced heating. It is recommended that temperature rise should be used to evaluate the RF-induced heating for an AIMD lead.

Table 3-1. Peak local SAR_{1g} values and temperature rises at different electrodes

Lead Length (mm)	Electrode Size (Circle)	Peak SAR_{1g} (W/kg)	Temperature Rise (°C)	Reduction Percent
	0.25	83.79	13.4	0
150	0.50	91.20	11.6	13.43
	0.75	93.41	10.7	20.15
	0.25	169.53	27.0	0
200	0.50	193.03	24.1	10.74
	0.75	202.79	22.5	16.67
	0.25	296.69	45.4	0
250	0.50	342.97	41.2	9.25
	0.75	364.06	38.8	14.54

3.4 Numerical Validation

To validate the effectiveness of the electrode with large radial contact in reducing the RF-induced heating, three groups of leads with different trajectories were assessed in this section. The three groups of lead configurations are: (1) the straight lead group, (2) the L-shape lead group, and (3) the U-shape lead group as shown in Figure 3-6. Each group contains three different locations, which are 2 cm, 8 cm, and 10 cm from the inner wall of the ASTM phantom.

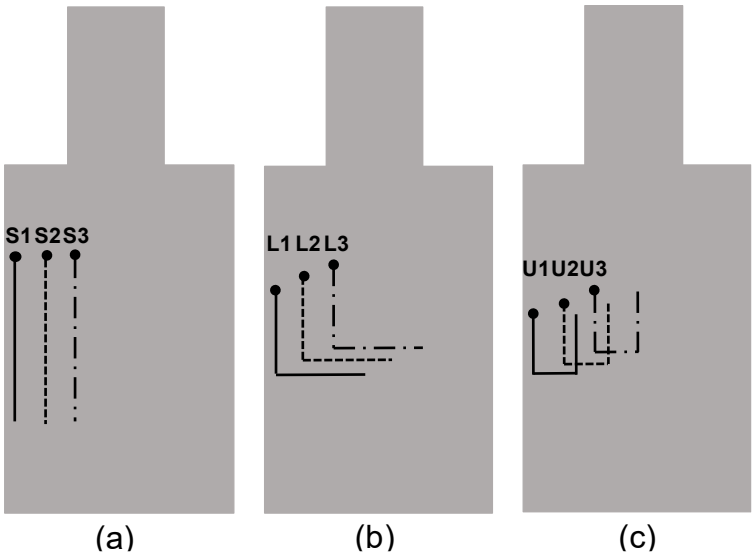

Figure 3-6. The lead pathways of (a) straight lead group (Distance to the left border: S1 = 2 cm, S2 = 6 cm and S3 = 10 cm). (b) L-shape lead group. (c) U-shape lead group.

The simulated temperature rises at the electrodes were plotted in Figure 3-7. It is found that for all positions, the temperature rise is decreased as the electrode size increases. This indicates that the dependence of the RF-induced heating to the electrode size will not change with the lead locations. It is also shown in Figure 3-7 that as the distance between the lead and the left border increases from 2 cm to 10 cm, the RF-induced heating near the electrode will decrease. This is because the incident electric field decays to the center of the ASTM phantom.

(a)

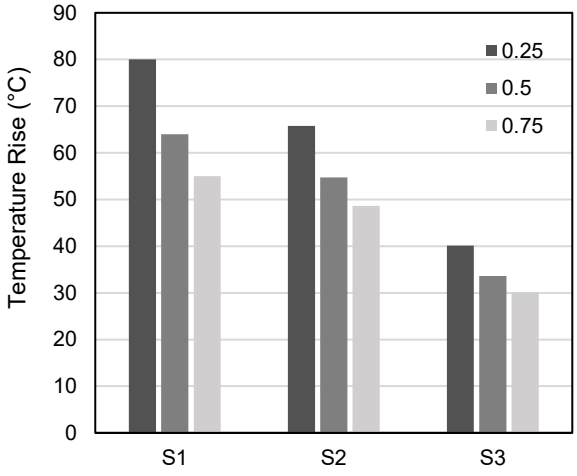

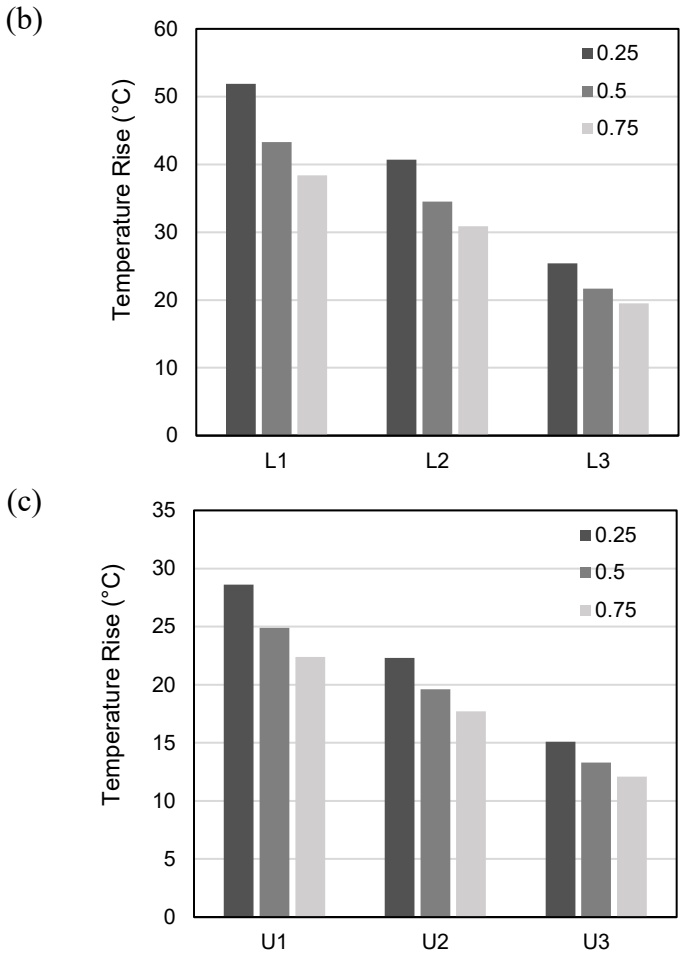

Figure 3-7. Computational temperature rises near the electrodes for (a) Straight lead group (b) L-shape lead group and (c) U-shape lead group.

3.5 Experimental Validation

In addition to the numerical investigation, experimental measurements have been performed to validate the effectiveness of the large radial contact in reducing the RF-induced heating for the implanted lead.

During the experiment, a copper wire was used to represent the AIMD lead. The inner copper conductor of the wire has a length of 270 mm and a diameter of 0.8128 mm. The outer insulation of the wire has a length of 260 mm and a thickness of 0.4064 mm. Thus, the bare tip of the wire is 10 mm. Three different sizes of copper foils were attached to the exposed wire to represent the electrode, as shown in Figure 3-8.

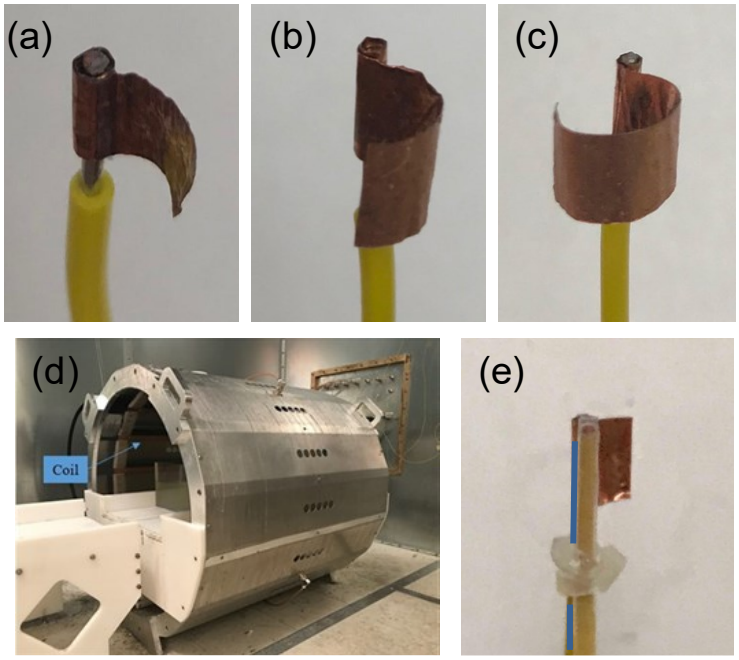

Figure 3-8. Lead electrodes used in measurements (a) a 0.25-circle electrode, (b) a 0.5-circle electrode, and (c) a 0.75-circle electrode. The 1.5 T MRI coil system for the thermal measurements is shown in (d), and (e) shows the optical-fiber thermal probe (blue line) connected to the generic electrode.

The copper wire was then placed in the ASTM phantom and exposed in an MRI RF coil for 15 min. The temperature was recorded 1 min before the RF power was turned on and continuously recorded for 2 min after the RF power was turned off. As shown in Figure 3-8(e), the thermal probe was bonded to the tip of the lead, while the highest temperature rise is near the edge of the cuff electrode.

Figure 3-9 shows the temperature rise as a function of time for the three electrodes, obtained from both numerical calculations and experimental measurements. As shown in Figure 3-9, enlarging the radial contact of the electrode from 90° to 270° reduces the temperature rise from 58.2 °C to 42.2 °C in the experiments, which agrees well with the simulated result. This result again demonstrated that a large electrode tends to mitigate the RF-induced heating of the implanted lead.

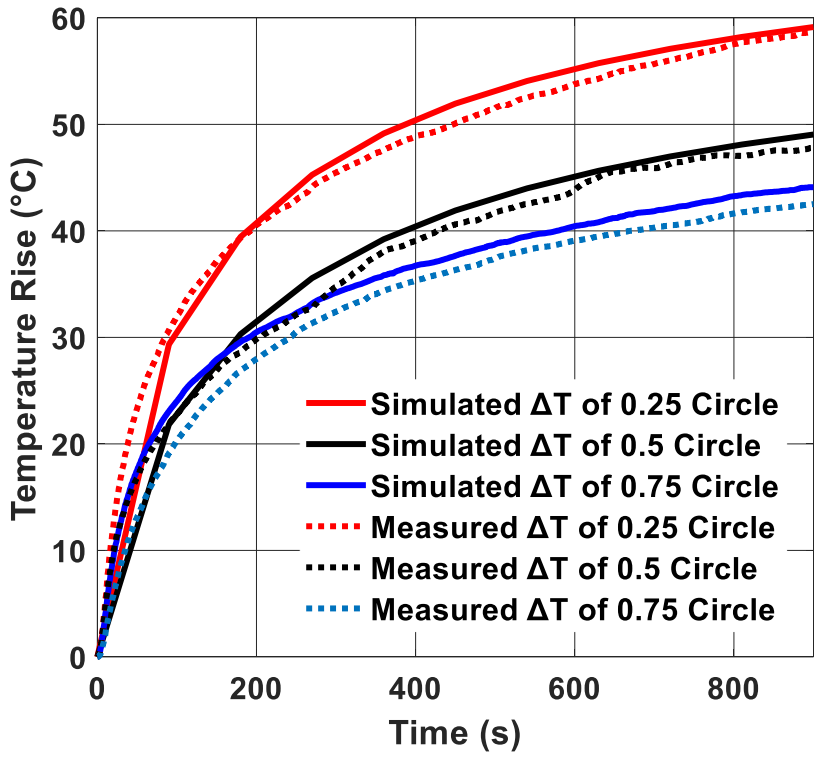

Figure 3-9. The temperature rises near the three electrodes. The solid lines indicate the simulated results, while the dash lines represent the measured results.

In addition to the temperature measurement, the transfer functions of three electrodes were also extracted both computationally and experimentally. For both simulated and experimental results, the magnitude plot is normalized using the maximum magnitude of the 0.25-circle transfer function.

Figure 3-10 (a) shows the transfer function magnitudes of the three leads with different electrode sizes. The solid lines refer to the simulated results and the dash lines refer to the measured results, which shows good agreement between the simulated and the measured results. Both results indicate that increasing the contact of the lead electrode will effectively reduce the magnitude of the transfer function without changing its shape.

Figure 3-10 (b) shows the transfer function phases of the three leads with different electrode sizes. Both results show that the leads with three different electrodes have a

similar phase shift. The total phase variations along the leads are within 10°, which is insubstantial. The slight disagreement between simulations and experiments could be due to the vibration of the lead when the current probe, driven by an electric motor, is moving along the lead body.

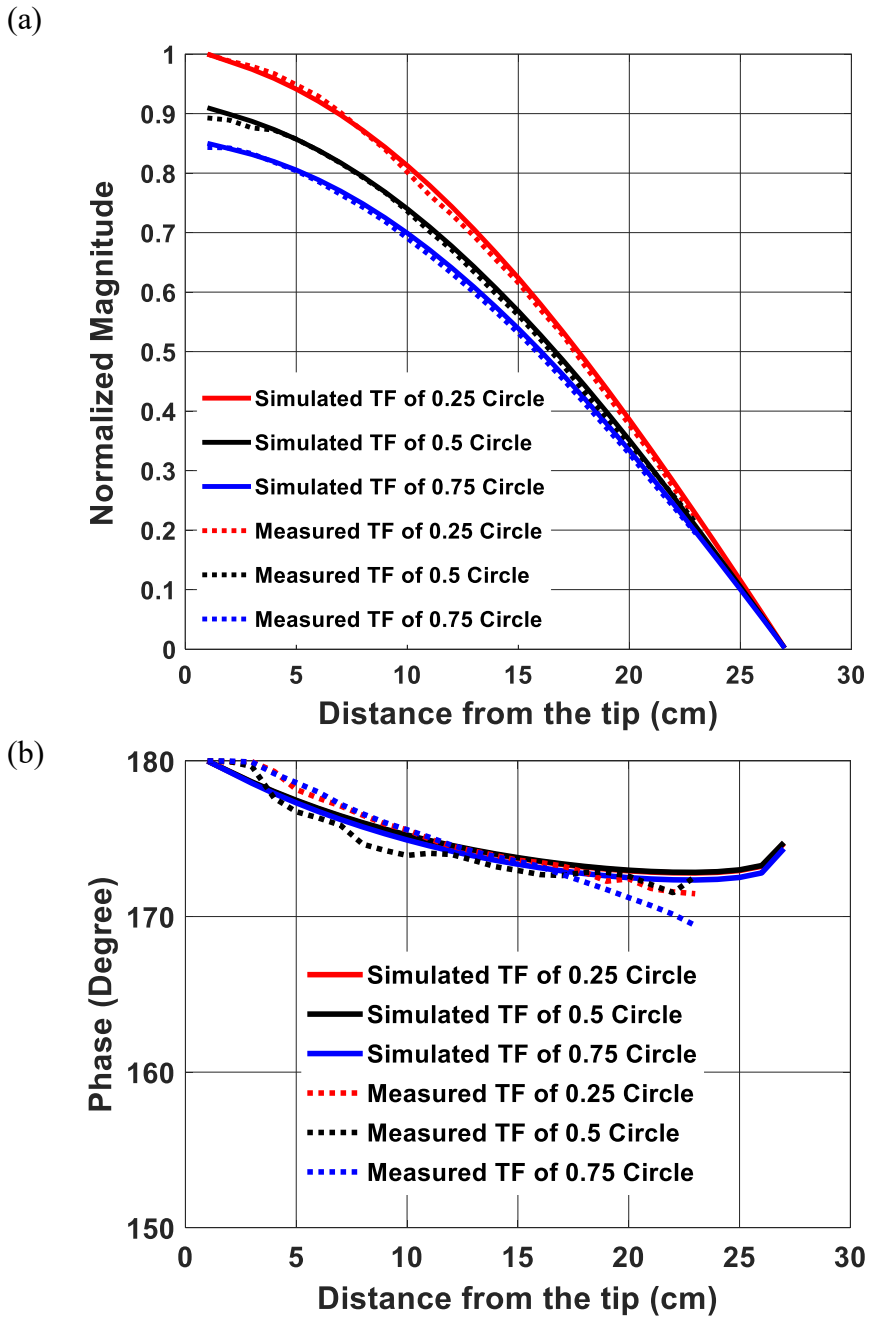

Figure 3-10. (a) The magnitude of the transfer function for three different electrode sizes. (b) The phase of the transfer function for three different electrode sizes.

During the experiment, there are a lot of factors that can influence the measured temperature rises at the device. To assess the quality of the experimental measurement, an uncertainty analysis was performed for parameters including the probe position, device position, and phantom parameters. Assuming linear dependence of the measurement values on the varying parameter, a sensitivity can then be determined for each parameter. Multiplying the sensitivity with the standard deviation of the parameter produces the uncertainty of this parameter. Considering that the parameters are independent of each other, the overall uncertainty can be calculated as the root-sum-square of the individual parameters. Table 3-2 shows the uncertainties of different parameters during the experiments.

Table 3-2. Summary of standard uncertainties for the temperature measurement

Uncertainty Source	Sensitivity	Standard Deviation	Uncertainty (%)	Combined Uncertainty (%)
Probe Position	10.81 %/mm	$1/\sqrt{3}$ mm	6.24	8.98
Device Position	6.15%/mm	$1/\sqrt{3}$ mm	3.55	
Phantom Parameter	0.54 %/%	10%	5.4	

3.6 Discussion

In previous studies, most studies were focused on the structure of the lead body. For example, it was demonstrated in [40] that adding a coil to the lead can reduce the 10-gram averaged SAR (SAR_{10g}) from 9.6 W/kg to 4.2 W/kg while installing pins along the lead body leads to a lower SAR_{10g} of 2.6 W/kg in 1.5 T MRI. In particular, the temperature rise of the lead at 1.5 T can be reduced from 17.1 °C to only 1.7 °C using optimum pin number and optimum pin dimensions. However, this method increases the difficulty of manufacturing and reduces the long-term reliability of the lead. In addition

to refining the structure of the lead body, it was shown in [42] that the normalized peak SAR around the lead tip is 73.5% lower with the high permittivity material helmet than without it. To achieve this heating reduction effect, the relative permittivity of the material was selected to be 600. Although it is possible to achieve such high relative permittivity using ceramic, this material is solid and not flexible.

In our work, enlarging the electrode size from 0.25 circle to 0.75 circle reduces the RF-induced heating from 58.2 °C to 42.2 °C. The simulation results show a temperature reduction of 31.25% near the electrode edge and 26.06% at the lead tip, and the experimental results show a reduction of 27.49% at the lead. Although the effect of heating reduction by modifying the electrode structure is not as good as other techniques, it can be used in combination with other methods to make an MRI-compatible AIMD for patients.

Moreover, a single conductor was used to model the AIMD lead. The transfer function of a single-conductor lead was simulated and measured. It is found that a large electrode size can reduce the magnitude of the transfer function. This indicates that enlarging the contact of the electrode can reduce the energy deposition rate at the electrode, subsequently decreasing the heating effect. However, in real clinical applications, the number of cuff electrodes is more than one and each cuff electrode is connected to a lead conductor. Therefore, it is essential to investigate the effectiveness of a large electrode size for the multi-conductor leads. For multi-conductor leads, we can still use the Huygens equivalent principle and the reciprocity theorem to estimate the electric field at the lead tip.

3.7 Summary

In summary, this study demonstrates that increasing the radial contact of the electrode can effectively reduce the RF-induced heating of the AIMD lead. By increasing the electrode to a 270° circle, the simulation results show a temperature reduction of 31.25% near the electrode edge and 26.06% at the lead tip, and the experimental results show a reduction of 27.49% at the lead tip. This result illustrates that the strategy of enlarging electrode size can reduce the RF-induced heating for AIMD leads and broaden the safe imaging conditions for patients with implants. Despite reducing the heating, the largest electrode (0.75 circle) still shows a temperature rise of 42.2 °C from the experiment. It is worth noting that this value does not indicate the real temperature rise in a human body with blood flow and an inhomogeneous medium [50]. The blood perfusion inside the human body will reduce the heating effect further in a patient [51]. Although the temperature rises obtained by calculations and measurements cannot represent the real heating situation in the human body, the heating-reducing effect benefiting from the large electrode size is expected to be the same in a patient. Also, together with other techniques for heating reduction, such as optimization of the lead body [39], [52] or the application of a high dielectric pad [53]-[55], an AIMD can be made even safer in the MRI process.

The mechanism of heating reduction by a large electrode contact is also investigated in this study. Unlike adding a coil and adding pins in the lead [40], which reduces the RF-induced heating by preventing the RF energy from delivering to the electrode, enlarging the radial contact of the electrode can reduce the heating effect by decreasing the energy deposition density at the electrode. It should be noted that the

effect of the electrode modification on the performance of the lead and the associated stimulating system was not explored as part of this study. This potential issue needs further investigation.

In conclusion, we have shown that a minor modification to a lead electrode substantially reduces the RF-induced heating of the AIMD lead. Because this electrode modification changes the SAR distribution at the electrode, it is expected that similar results will apply to longer leads and multi-conductor leads. These findings provide a general guideline in the electrode design aiming to reduce the RF-induced heating of AIMDs. Also, it is found that compared with local SAR_{1g}, it is more reliable to use temperature rise when evaluating the RF-induced heating risk of medical implants with fine structures, such as AIMDs.

Chapter 4

Reducing RF-induced Heating for the External Fixation using Capacitive Structures

4.1 Background

In addition to AIMDs, another type of medical implants that can cause severe heating effect is the external fixation device [9]. To mitigate the RF-induced heating of the external fixations, Liu et al. proposed to use insulating material to prevent the propagation of RF energy from the device frame to the pin tips [35]. They showed that applying proper insulating material could reduce RF heating by 67% at 1.5 T. Huang et al. improved this method by changing the insulating material to the absorbing material [56]. This material could absorb part of the RF-induced energy on the device frame, so it would reduce the heating effect in the human body. Although these studies achieved good results in mitigating the RF-induced heating of the external fixation, there are some limitations associated with their studies. First, these studies only investigated the effects of the relative permittivity on the RF heating and failed to consider the effects of other parameters such as the thickness of the insulating material. Second, their methods were only demonstrated at 1.5 T MRI. As high field MRI is widely used in clinical, there arises a need to investigate the effectiveness of the insulating/absorbing material in reducing RF heating of the external fixation devices at 3 T MRI. Finally, yet importantly, it is essential to illustrate the fundamental reason why insulating/absorbing material can reduce RF-induced heating of the external fixation, and to develop a general method which can reduce the RF heating for various device combinations at both 1.5 T and 3 T.

In this study, the effects of the insulating material on external fixation devices at 3 T MRI were investigated. While applying a thin insulating layer with low dielectric constant around the pins can reduce the RF-induced heating of the external fixation in 1.5 T MRI., the direct application of this method led to increased heating at 3 T MRI. To clarify the heating mechanism of the external fixation device and develop a general heating reduction method, an equivalent circuit model was developed. It shows that the most critical design for heating reduction is to detune/mitigate the coupling between the external fixation devices and the RF fields from MRI systems. Carefully designed capacitive structures were then developed to investigate this strategy. Numerical simulations were performed to verify the validity of the circuit model and the proposed method to reduce the RF-induced heating of the external fixation device. Further experiments were conducted to demonstrate the effectiveness of the proposed method in reducing RF-induced heating for external fixation devices at 1.5 T and 3 T.

4.2 Circuit Model

To illustrate the heating mechanism of the external fixation device under the MRI RF exposure, an equivalent circuit was developed as shown in Figure 4-1. The RF power coupled to the external fixation device is modeled as a voltage source, which is mainly determined by the dimensions of the device [57], [58]. The metallic device is modeled as an inductance due to the low conductive loss for this kind of device. Since the human body dissipates the most RF energy [59], four resistors are used to represent the tissues around the four pins [60]. The four resistors are connected in parallel, according to the structure of the external fixation device.

It should be noted that the two metallic screws on the same side can generate extra capacitance as immersed in the conducting medium. However, considering that the RF frequency in the MRI machine is not very high and the distance between the two screws is 60 mm, the parasitic capacitance was ignored in this study.

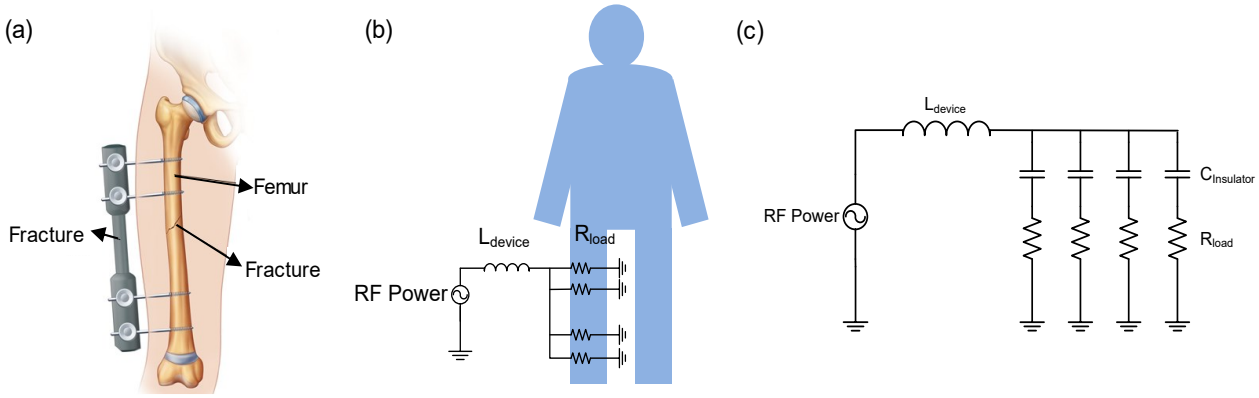

Figure 4-1. (a) An external fixation screwed into the fractured tibia, (b) A lumped circuit model to illustrate the heating mechanism of the external fixation device, (c) Circuit model for the external fixation with insulating material.

According to the circuit theory, the dissipated power near the pin tips can be calculated as

$$P = I^2 R_{load}, \tag{7}$$

where I is the induced current on the external device and is calculated by

$$I = \frac{V_{RF}}{j\omega L_{device} + R_{load}}, \tag{8}$$

where R_{load} is the equivalent resistance of the four resistors in parallel.

The induced current flowing on the screws was plotted in Figure 4-2. As we can see, for screws on the same side, the current is a common mode type, flowing equally in the two paths. For screws on different sides, the current is a differential loop type. It flows into the gel through the screws on one side and returns through the screws on the

other side. This is set up by the EMF around the loop due to the changing magic flux through the loop path.

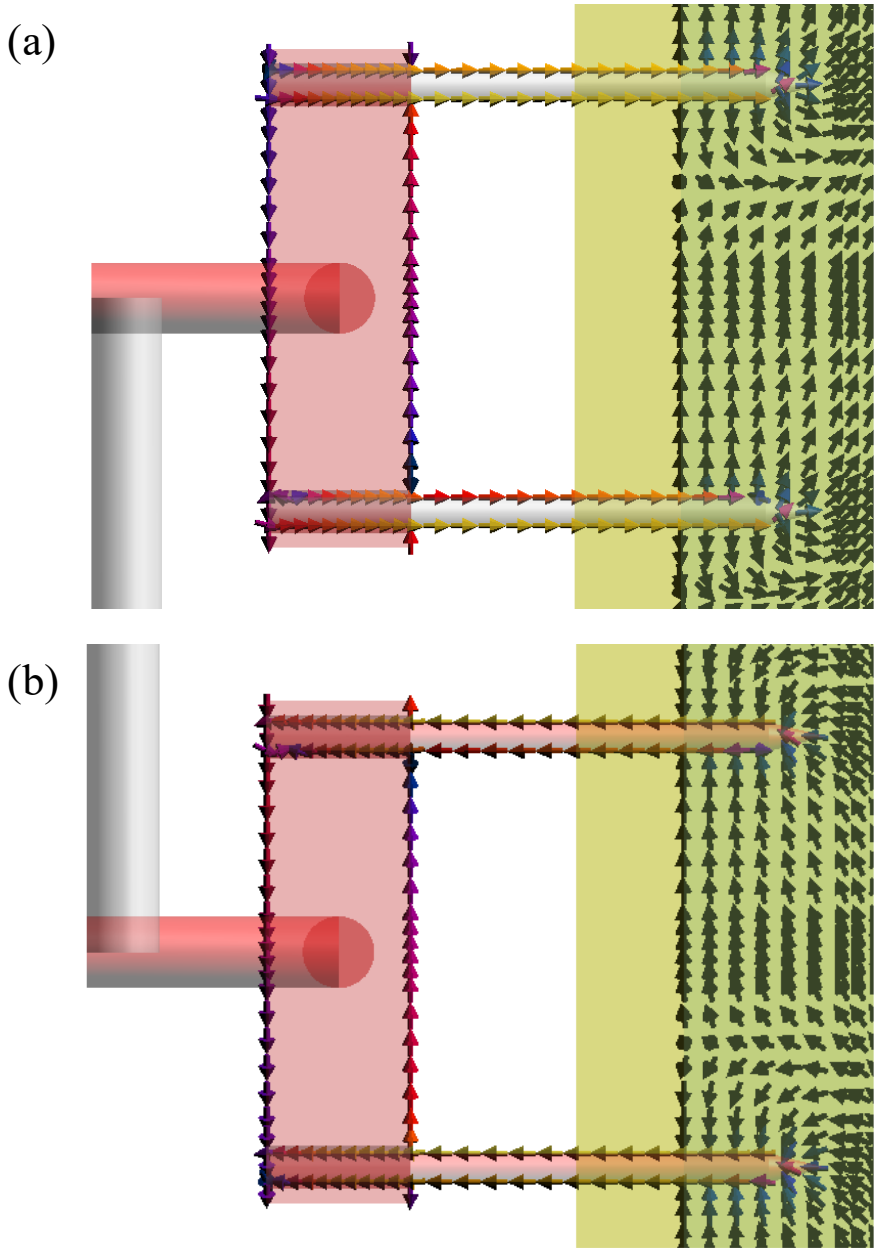

Figure 4-2. Current distributions on (a) the two screws above, and (b) the two screws below.

If the total equivalent impedance of the external fixation device is increased, the dissipated power by the load near the pin tips will decrease as well. In other words, any structures that add extra additive resistance, capacitive reactance or inductive reactance,

or a combination of these impedances to the circuit can reduce the RF-induced heating of the external fixation. Compare to other options, the capacitive structure is easier to implement, and has less effect on the mechanical properties of the external fixation devices. Therefore, the capacitive structure is used in this study.

A typical way to introduce capacitive impedance is to place an insulating material between two adjacent metallic faces. If the insulating material is lossy, it will introduce complex impedances including resistance and capacitive reactance. In this study, the insulating material is used as an example. After inserting insulation material between the joints of pins and clamps, the circuit model is modified as shown in Figure 4-1(c). The equation to calculate the induced current on the device is then revised as

$$\mathrm{I} = \frac{V_{RF}}{j\omega L_{device} + \frac{1}{4}\left(\frac{1}{j\omega C_{insulating\ cover}} + R_{load}\right)}. \tag{9}$$

The capacitance of a cylindrical capacitor is calculated by

$$\mathrm{C} = \frac{2\pi\varepsilon_0\varepsilon_r h}{\ln(b/a)}, \tag{10}$$

where a, b and h are the inner radius, outer radius, and height of the medium, ε_r is the relative permittivity of the material.

The inductive reactance generated by the device and the capacitive reactance induced by the insulating material together contributes to the total impedance of the device. According to the modified circuit model, if the total impedance of the device is increased, the induced current flowing to the human body will be decreased. As a result, less RF power will be dissipated near the pin tip and the heating effect will be mitigated as well.

4.3 Numerical Investigation

4.3.1 Simulation Settings

Without loss of generality, a tibia external fixation model was built as shown in Figure 4-3. It consists of three parts: (1) two metallic blocks to represent the clamps, (2) two straight rods to connect the clamps, and (3) four pins to be inserted into the human body. The clamp block has dimensions of 70 mm × 15 mm × 20 mm. The connecting rod has a diameter of 10 mm and a length of 250 mm. The pin has a diameter of 4 mm and a length of 78 mm, with an insertion depth of 2 cm from the surface of the phantom. These dimensional parameters are obtained from a commercial external fixation device. Compared with the real external fixation device, our designed model ignores some structural details, such as the threads on the screw tip. This is acceptable because the wavelength of the RF field in MRI is much larger than the screw thread. Using the simplified external fixation model can speed up the convergence time of the electromagnetic simulation. The device is placed in the phantom as shown in Figure 4-4.

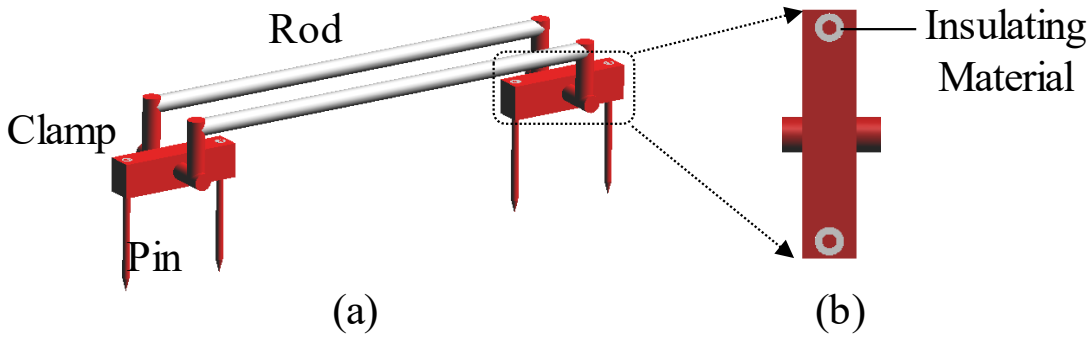

Figure 4-3. (a) Generic model of the external fixation used in this investigation. (b) Insulating material between the clamp and screw (the gray part).

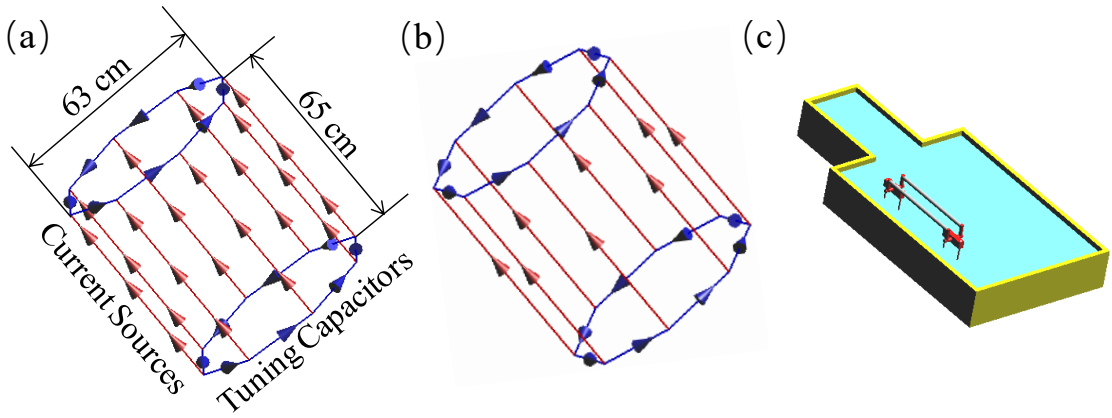

Figure 4-4. (a) Model of RF coil operating at 3 T, (b) Model of RF coil operating at 1.5 T, (c) Placement of the external fixation in the ASTM phantom.

4.3.2 Effect of the relative permittivity

First, the effect of the relative permittivity of the insulating material on the RF-induced heating is studied. In the initial setting, the insulating material is only inserted between the pins and clamps and has a fixed thickness of 2 mm. Figure 4-5 shows the peak SAR_{1g} varied with the relative permittivity of the insulating material. The peak SAR for the external fixation without insulating material is also plotted for reference. It is found that decreasing the relative permittivity of the insulator will reduce the heating in 1.5 T MRI, which is consistent with previous studies. However, it will increase the heating in 3 T MRI. As the relative permittivity of the insulating material goes down to 2, the peak SAR_{1g} will decrease from 752 W/kg (without pin covers) to 61 W/kg at 1.5 T, while it will increase from 388 W/kg (without pin covers) to 850 W/kg at 3 T.

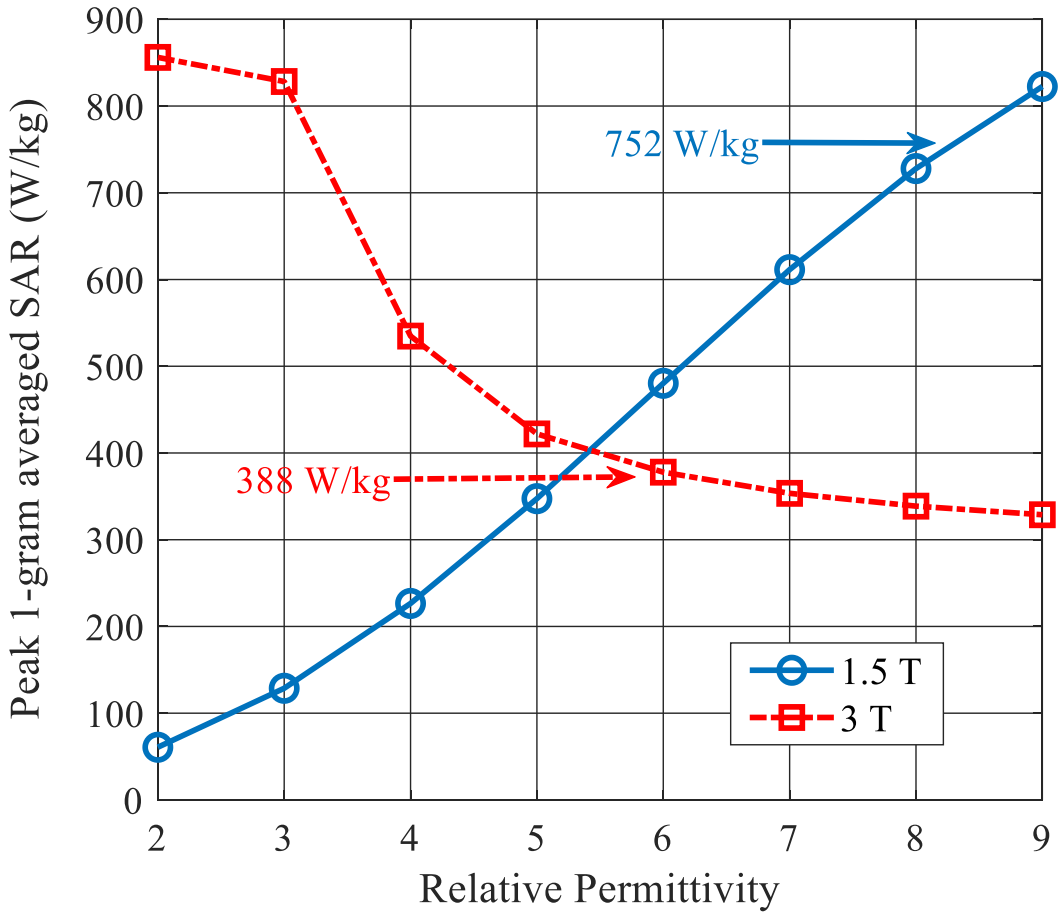

Figure 4-5. Peak SAR_{1g} of external fixation varied with relative permittivity of the insulator at 1.5 T (Blue solid line) and 3 T (Red dash line). The blue and red arrows indicate the heating levels of external fixation without insulating material at 1.5 T and 3 T, respectively.

Figure 4-6 shows the simulated local SAR_{1g} distributions for the external fixation devices without insulating material and with insulating material with a dielectric constant of 2. In this figure, 0 dB corresponds to the peak SAR_{1g} value of the external fixation without pin covers. For 1.5 T, the value is 752 W/kg. For 3 T, this value is 388 W/kg.

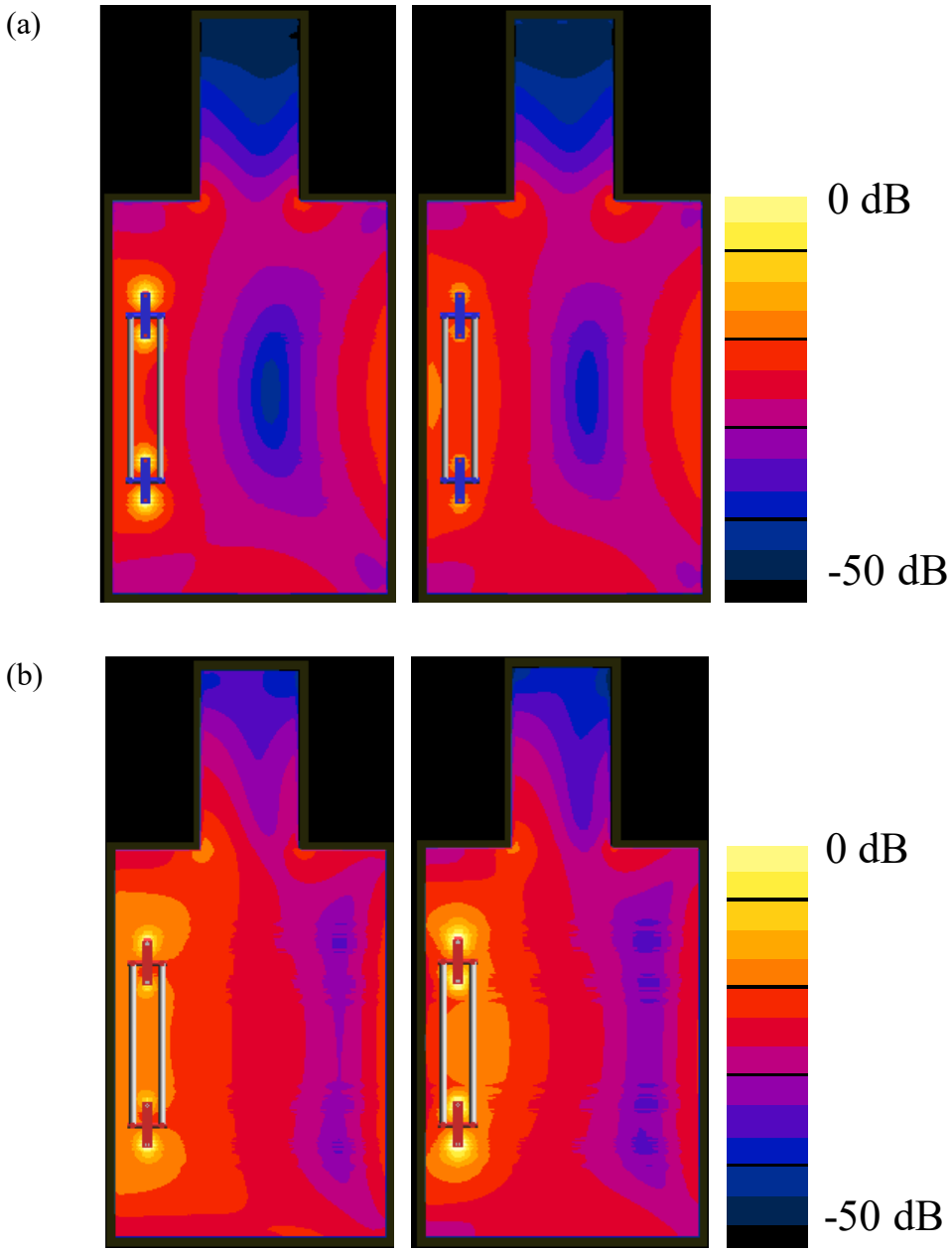

Figure 4-6. Simulated local SAR_{1g} distributions in the ASTM phantom with traditional external fixation device (left) and modified external fixation device (right) at (a) 1.5 T, and (b) 3 T.

This fact can be illustrated by the circuit model in Figure 4-1. At 1.5 T, the working frequency of the RF coil is 64 MHz. The inductive reactance generated by the device is insubstantial, which can be easily compensated by the capacitive reactance from the insulating material. As the relative permittivity of the insulating material decreases,

the capacitive reactance from the insulating material will increase, subsequently increasing the total impedance of the device and preventing the induced current from flowing into the load. Therefore, less power is dissipated by the gel and less heating is induced.

As the frequency is increased to 128 MHz at 3 T, the inherent inductive reactance of the device is increased and becomes significant. Increasing capacitive reactance will offset the inductive reactance, which eventually reduces the total impedance of the device. Therefore, a low dielectric constant that induces a large capacitive reactance will lead to higher RF-induced heating at 3 T MRI.

As shown in Figure 4-5, as the relative permittivity of the insulation layers goes to 2, the worst heating at 3 T will occur. According to the circuit model, the worst heating is generated when the device is in the resonance mode. As the added capacitive reactance exactly cancels the inductive reactance of the circuit, the induced current will reach the maximum value, causing severe heating near the pin tip. To validate the resonance frequency of the external fixation device with insulation layers, eigenmode analysis was performed using HFSS. For this model, only the first mode was computed. For maximum accuracy, curvilinear elements were used. Simulated results show that the resonance frequency of the device is 121.70 MHz, which is very close to the RF frequency (128 MHz) in 3 T MRI. The quality factor (Q) of the device is computed as 1.49. The low Q value indicates the large energy loss from the conductive phantom gel.

4.3.3 Effect of the Thickness

In this section, the effect of insulating layer thickness on the RF-induced heating was investigated and the result was plotted in Figure 4-7.

(a)

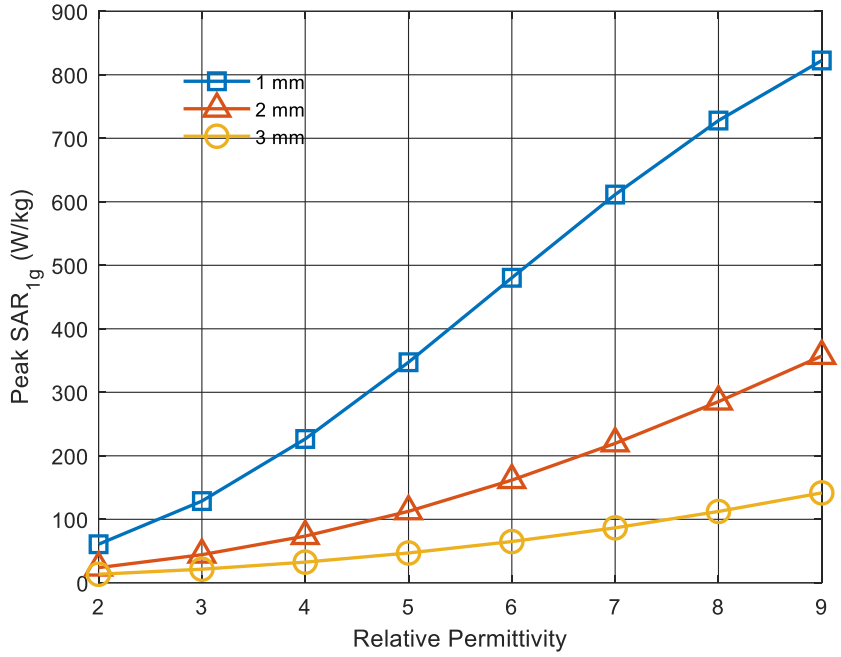

(b)

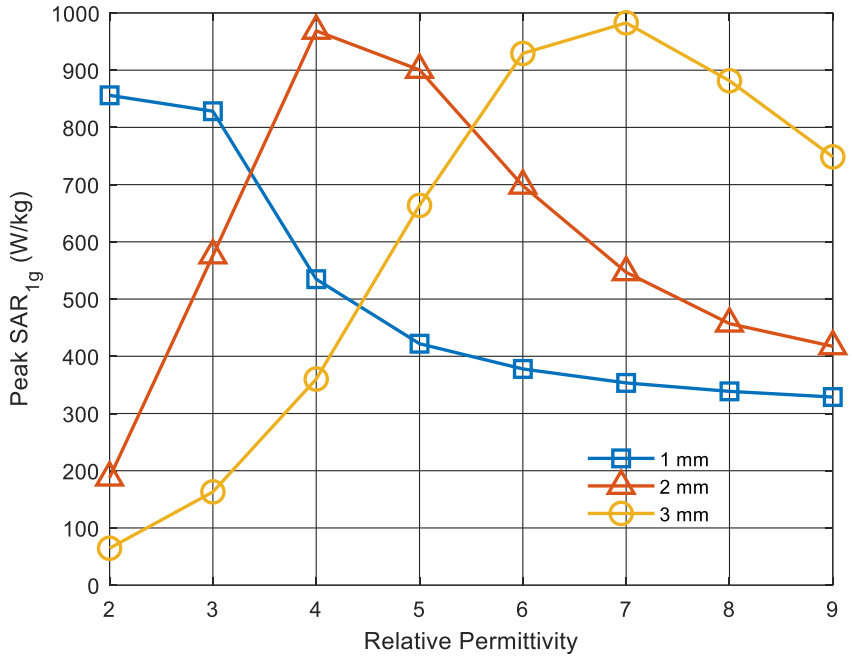

Figure 4-7. RF-induced heating varied with the thickness of the insulating layer at (a) 1.5 T MRI, (b) 3 T MRI.

At 1.5 MRI, the RF-induced heating is decreased as the thickness increases from 1 mm to 3 mm. This fact also can be explained by the circuit model. According to

Equation (10), the capacitance introduced by the insulating layer will decrease with the thickness of the insulating layer. Moreover, a smaller capacitance leads to a larger capacitive reactance, which prevents the RF-induced current from flowing into the lossy gel. Therefore, less RF energy is concentrated near the pins of external fixation devices and the RF-induced heating is subsequently mitigated as well.

Compared with 1.5 T MRI, the RF-induced heating is not necessarily decreased at 3 T MRI by increasing the thickness of the insulating layer. It is found that the worst case of RF-induced heating shifts as the thickness increases for 3 T MRI. This finding is consistent with the proposed circuit model. As analyzed above, the worst case of heating happens when the introduced capacitive reactance exactly offsets the inductive reactance of the circuit. For a specific external fixation device, the capacitance needed to make the equivalent circuit of the external fixation resonate is constant. After increasing the thickness of the insulating layer, to obtain the same capacitance, the relative permittivity of the insulating material also increases. Therefore, the worst-case heating shifts towards a higher relative permittivity as the thickness of the insulating layer increases. When the thickness of the insulating material increases to 3 mm, the RF heating of the external fixation at 3 T can be mitigated to a peak local SAR_{1g} of 64.53 W/kg by applying insulating material with a relative permittivity of 2. This indicates that as the insulating material is thick enough, a low dielectric constant can still reduce the RF heating of the external fixation in 3 T MRI.

The effects of the relative permittivity and the effects of the thickness on the RF-induced heating of the external fixation at different MR frequencies were investigated. Both results show that a single insulating layer with low relative permittivity cannot

ensure the heating reduction of the external fixation during the MR scan. The proposed circuit model can clarify the different effects of the insulating material at 1.5 T and 3 T.

4.3.4 Quantitative Analysis using Circuit Model

In the previous sections, it is concluded that the worst case of heating would occur when the introduced capacitive reactance exactly offsets the inductive reactance of the external fixation. Since the added capacitance can be calculated using Equation (10), the inherent inductance of the external fixation is estimated based on the following resonant condition

$$\omega^2 LC = 1. \tag{11}$$

Using the worst-case RF heating at 3 T from Figure 4-7, the inductance of the external fixation device is calculated and summarized in Table 4-1. As we can see, these values are close to each other.

Table 4-1. Calculated inductance using the circuit model at 3 T

Thickness (mm)	Inductance (nH)
1	58.44
2	60.20
3	59.34

The average value of the inherent inductance is 59.33 nH and we used this value to calculate the normalized power dissipated by the phantom. Figure 4-8 shows how the normalized power loss changes with the thickness and the relative permittivity of the insulating material. It is found that the results calculated by the circuit model are consistent with the results calculated by the numerical simulation. This fact again validates the proposed circuit model. This circuit model can help us estimate the inherent inductance of an external fixation device, which makes it easier to determine the required capacitance to detune the coupling between the external fixation device and the RF coil.

(a)

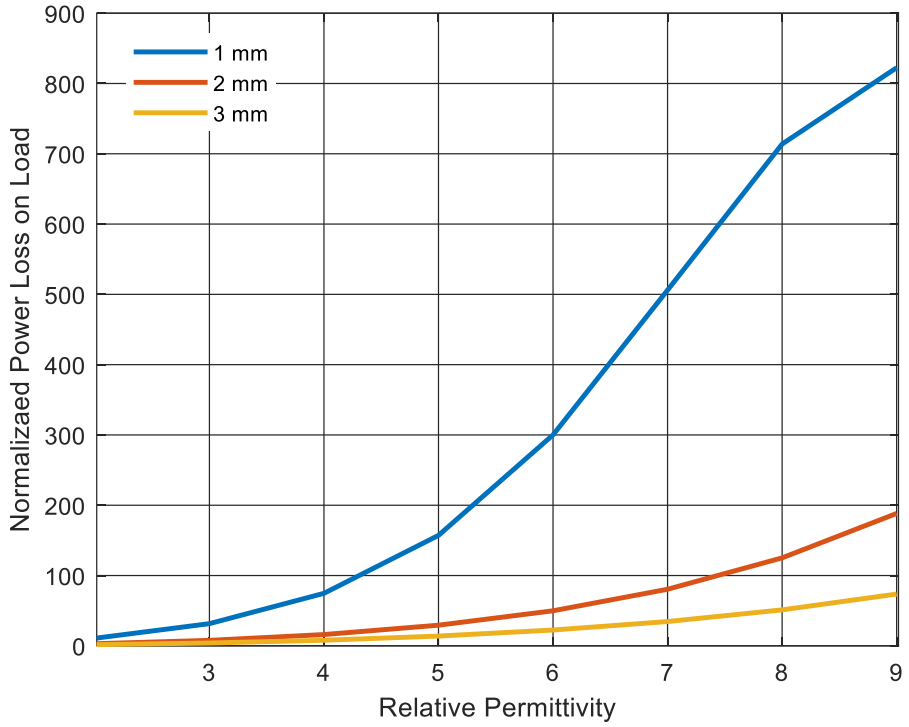

(b)

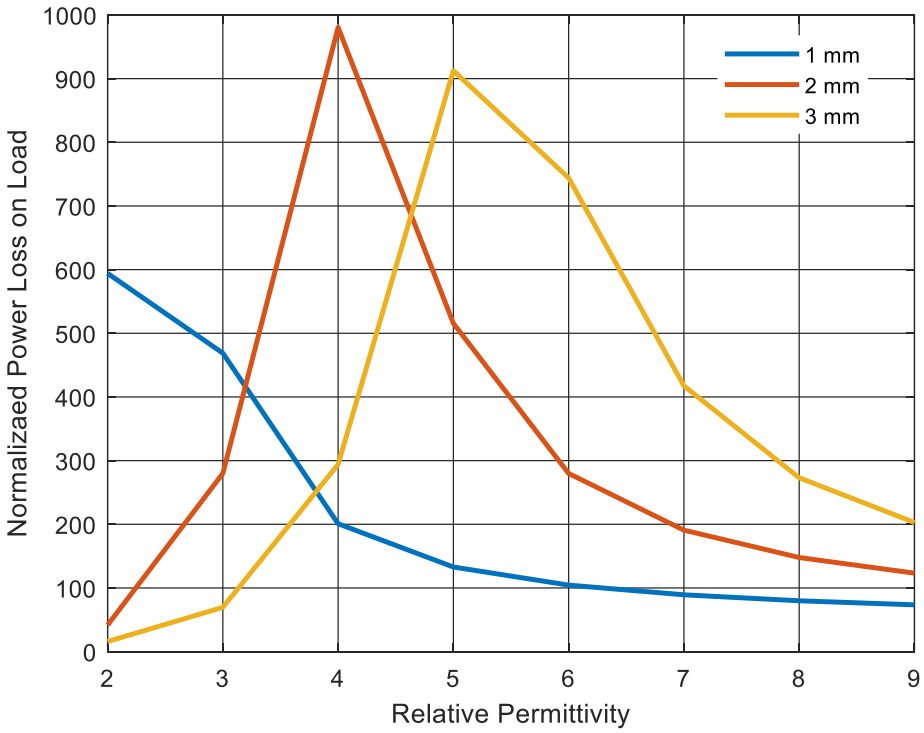

Figure 4-8. Normalized power loss on the load of the ASTM phantom versus relative permittivity using the circuit model.

4.3.5 Adding Inductance and Resistance

According to the circuit model, increasing the total impedance of the device is the key to reducing the RF heating of the external fixation. In other words, any structures that add extra additive resistance, capacitive reactance or inductive reactance, or a combination of these impedances to the circuit can reduce the RF-induced heating of the external fixation. In this section, the effect of introducing inductance and resistance to the external fixation device on the RF-induced heating was investigated.

As the inductive or resistive structures are difficult to implement, lumped elements that can represent the idealized inductors or resistors were used during the electromagnetic simulations. As shown in Figure 4-9, four lumped elements were inserted between the pins and clamps of the external fixation device. During the simulations, each lumped element is first set to be an inductor with 1000 nH. Then, it is set to be a resistor with 1000 Ω.

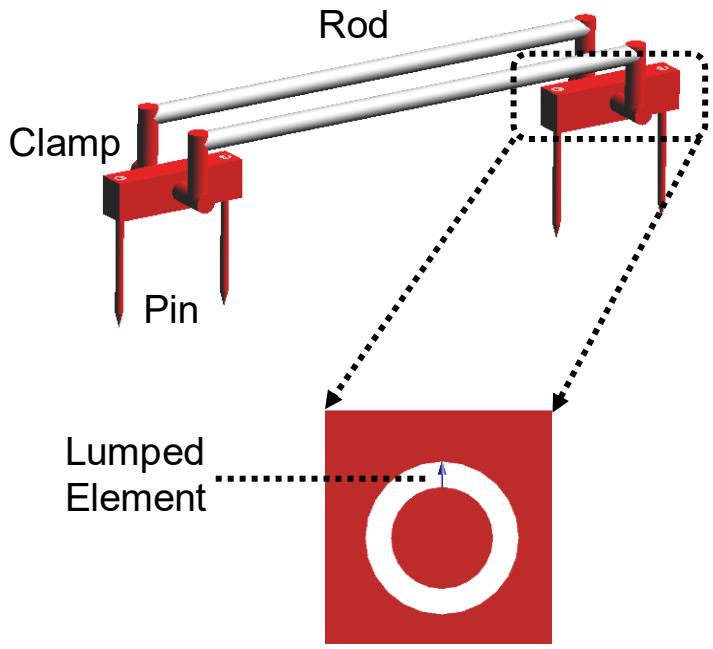

Figure 4-9. A lumped element which can add inductance or resistance of the external fixation device.

Figure 4-10 shows the local SAR_{1g} distributions in the ASTM phantoms when the external fixation device is introduced with inductance or resistance at both 1.5 T and 3 T. All the SAR values are normalized to the maximum SAR value in the phantom with the original external fixation device. For 1.5 T results, 0 dB represents 752 W/kg. For 3 T results, 0 dB represents 388 W/kg. As we can see from Figure 4-10, increasing the inductance or resistance can effectively reduce the RF-induced heating at both 1.5 T and 3 T. This finding demonstrates the validity of the proposed circuit model.

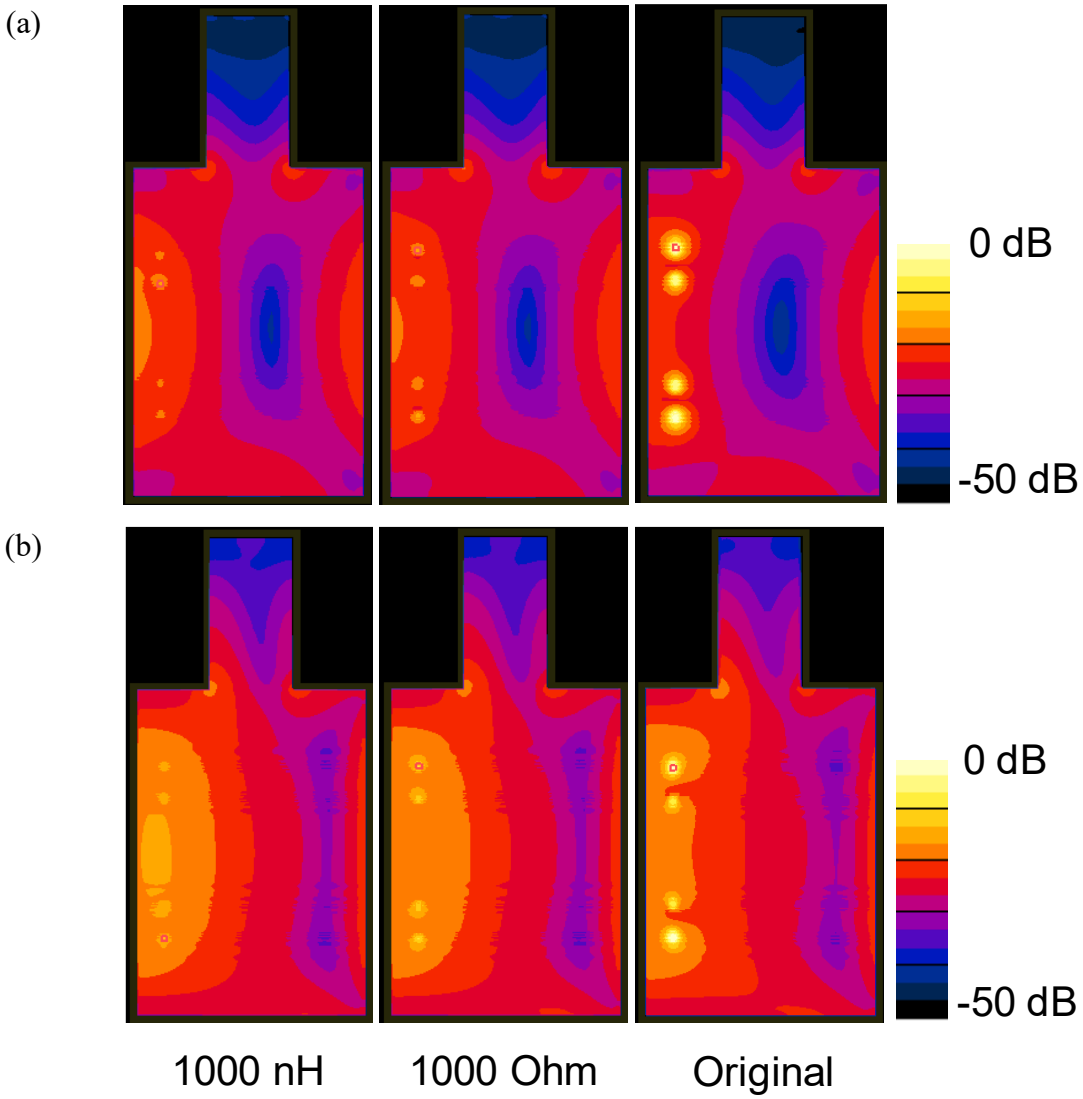

Figure 4-10. At (a) 1.5 T and (b) 3 T, the local SAR_{1g} distributions in the ASTM phantoms when introducing inductance, resistance and nothing to the external fixation device.

4.3.6 Adding More Capacitive Structures

Compare to other options, the capacitive structure is easier to implement, and has less effect on the mechanical properties of the external fixation devices. Therefore, the capacitive structure is used in this study. Due to the inherent inductance from the metallic device, the total impedance of the circuit is dependent on the difference between the capacitive reactance from the insulating material and the inherent inductive reactance. Therefore, we propose to add more capacitive structures to the external fixation device to minimize the RF-induced heating at 3 T MRI. The purpose of adding extra insulating layers is to introduce more capacitive reactance in series so that the remaining capacitive reactance is large enough to prevent the induced current from flowing into the pin tips after canceling the inherent inductive reactance. Specifically, extra insulating materials with a dielectric constant of 2 and a thickness of 2 mm were added in the joints of the rods and clamps in the simulations.

Figure 4-11 shows the peak SAR_{1g} for external fixations with various rod lengths at 1.5 T and 3 T. The blue bars indicate the heating of the device with no insulators, while the orange bars indicate the heating of the device with insulating covers on both pins and rods. At both 1.5 T and 3 T, adding more capacitive structures in the rod-clamp joints effectively reduces the RF-induced heating. Moreover, the heating reduction effect works for different rod lengths. For 1.5 T, the reduction effect ranges from 98.18% to 98.47%, with an average reduction of 98.35%. For 3 T, the reduction ranges from 93.56% to 95.90%, with an average value of 95.24%. This result again demonstrates the validity of our circuit model and the effectiveness of increasing the total impedance in mitigating the RF heating for the external fixation.

(a)

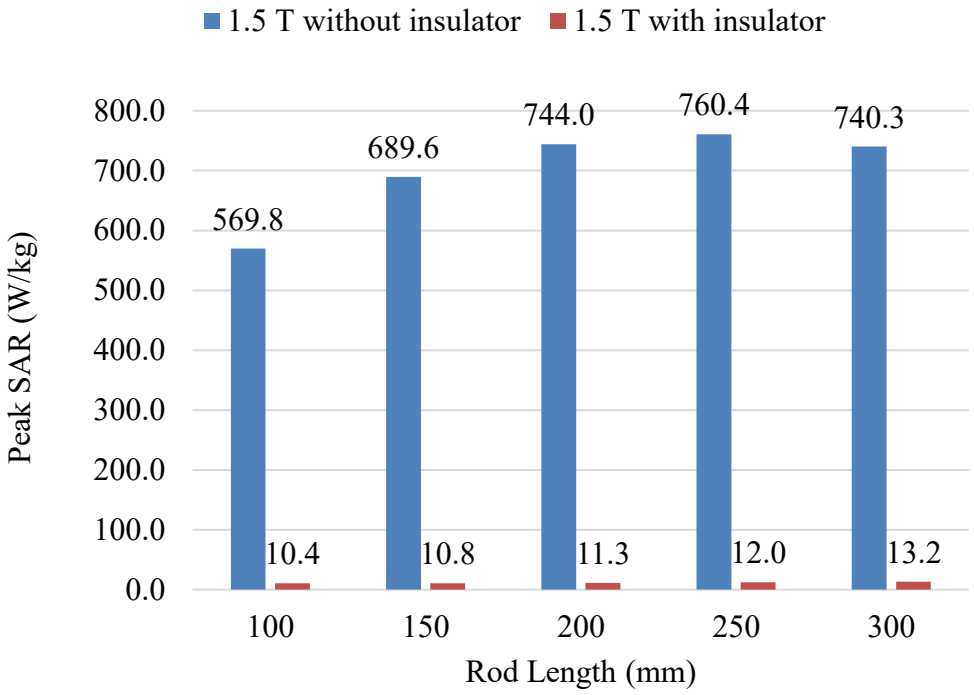

(b)

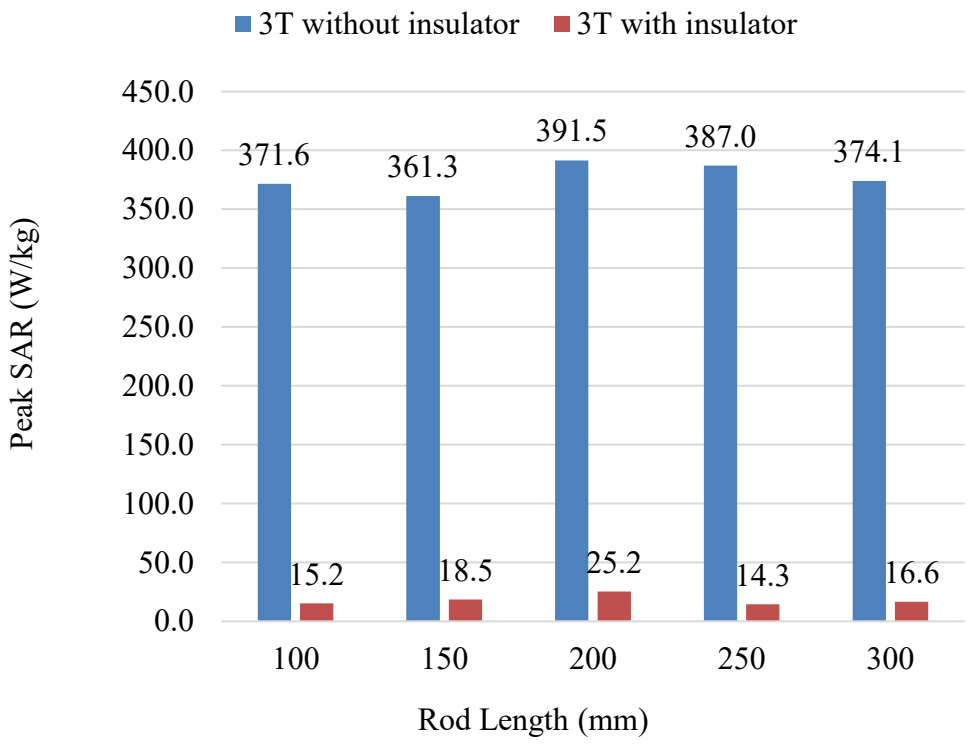

Figure 4-11. Peak SAR_{1g} of external fixation varied with rod length at 1.5 T and 3 T. The blues bars indicate the case without insulating covers, while the orange bars indicate the case with insulating covers on both rods and pins.

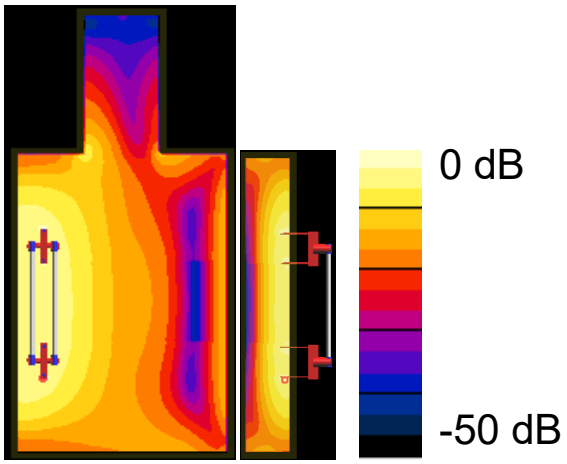

Figure 4-12. The local SAR_{1g} distribution for the external fixation device with both pin and rod insulations. 0 dB corresponds to the peak SAR_{1g} value of 14.3 W/kg.

Figure 4-12 shows the local SAR_{1g} distribution for the external fixation device after applying the insulations at both pins and rods at 3 T. As we can see, the peak SAR_{1g} value was reduced to only 14.3 W/kg.

Table 4-2. Summary of the peak local SAR_{1g} values for different insulations

Case	Peak SAR_{1g} at 3 T (W/kg)
No Insulations	388
Pin-only Insulations	856
Rod-only Insulations	587
Pin and Rod Insulations	14.3

We also investigated the RF-induced heating of the external fixation device with rod-only insulations at 3 T. The rod insulation layer has a thickness of 2 mm and a relative permittivity of 2, which is the same as the insulation layer at the pins. The peak local SAR_{1g} values of the external fixation device after applying different strategies have been summarized in Table 4-2. As we can see from Table 4-2, only the strategy of applying insulations at both rods and pins can reduce the peak local SAR_{1g} from 388 W/kg to 14.3 W/kg. Other methods including applying pin-only insulations and rod-only insulations will increase the heating at 3 T. These results also indicate that in high field

MRI, more capacitive structures are needed to decouple the interactions between the external fixation device and the RF field.

4.4 In-Vivo Validation

Since the human body is an inhomogeneous medium that is different from the ASTM phantom, it is essential to investigate the effect of the detuning method in the human body. In this section, Duke Model from the Virtual Family was used to validate the performance of the capacitive structures in reducing the RF-induced heating of the external fixation device. We selected a rod length of 250 mm. This length can cause a relatively high RF-induced heating and fit the tibia of Duke Model. The loading position of the human model was determined so that the external fixation is in the center of the birdcage coil. Three cases were compared namely Duke Model in the presence of the external fixation, Duke Model in the presence of external fixation with capacitive structures, and Duke Model without any medical devices.

Figure 4-13 shows the local SAR_{1g} distributions of Duke Model at both 1.5 T and 3 T. From left to right, each subfigure includes three cases: the normal external fixation device, the external fixation device with capacitive structures and no external fixation device. As we can see, the peak local SAR_{1g} in the human model with the traditional external fixation is much larger than the value in the human model with the modified external fixation and the value in the human model without external fixation. Moreover, the SAR distribution in the human model with the modified external fixation is similar to the distribution in the human model without any implants. These findings indicate that for both 1.5 T and 3 T MRI, the RF-induced heating of the external fixation is effectively mitigated by introducing enough capacitive structures.

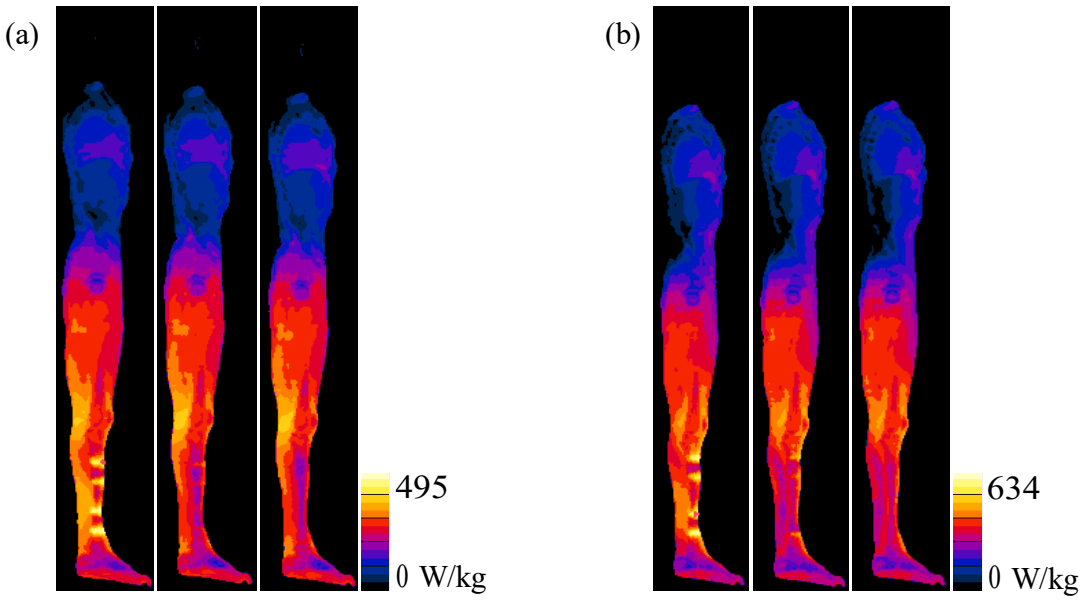

Figure 4-13. Local SAR_{1g} distributions of Duke model (a) at 1.5 T, and (b) at 3 T.

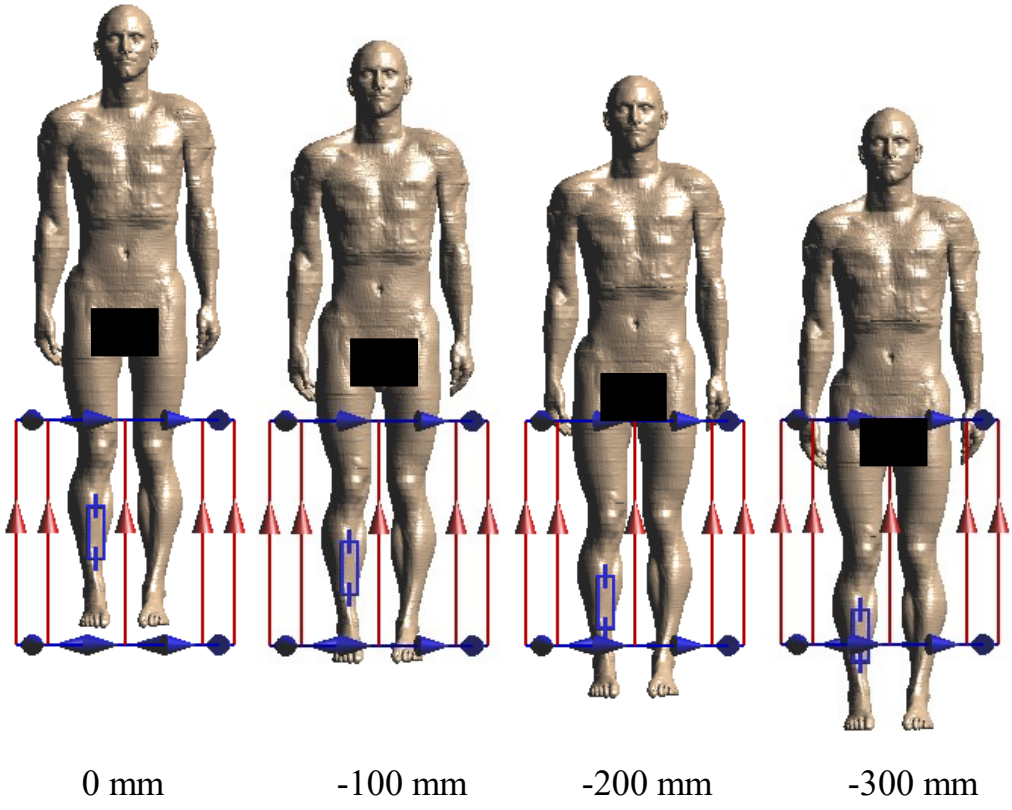

Figure 4-14. The loading positions of Duke Model with the external fixation device in the generic birdcage coil.

The effect of different loading positions is also investigated in this section. As shown in Figure 4-14, we refer to the loading position when the external fixation is at the center of the coil as 0 mm and then move the human model down every 50 mm. For each loading position, three EM simulations were performed: Duke model with the normal external fixation device, Duke model with the detuned external fixation device using capacitive structures, and Duke model without any external fixation device.

The peak local SAR_{1g} in the human model for each loading position is plotted in Figure 4-15. It is found that the RF-induced heating of the external fixation is reduced by the capacitive structures for every loading position in the study. Moreover, the RF-induced heating in the human model with a detuned external fixation almost overlaps with the heating in the human model without the external fixation. For the human model with a detuned external fixation device, the peak local SAR_{1g} will not even appear near the external fixation device. It usually occurs on the hand of the human model, which is the same as the human model without any external fixation device. This result is consistent with the SAR distribution result.

It is also found that the RF-induced heating is decreased as the loading position is increased. This is because the coupling between the external fixation device and the RF coil is reduced as the device moves out of the coil. Numerical simulations in this part again demonstrate that using capacitive structures can effectively detune the coupling between the external fixation device and the RF coil, subsequently reducing the RF-induced heating of the device in the human model.

(a)

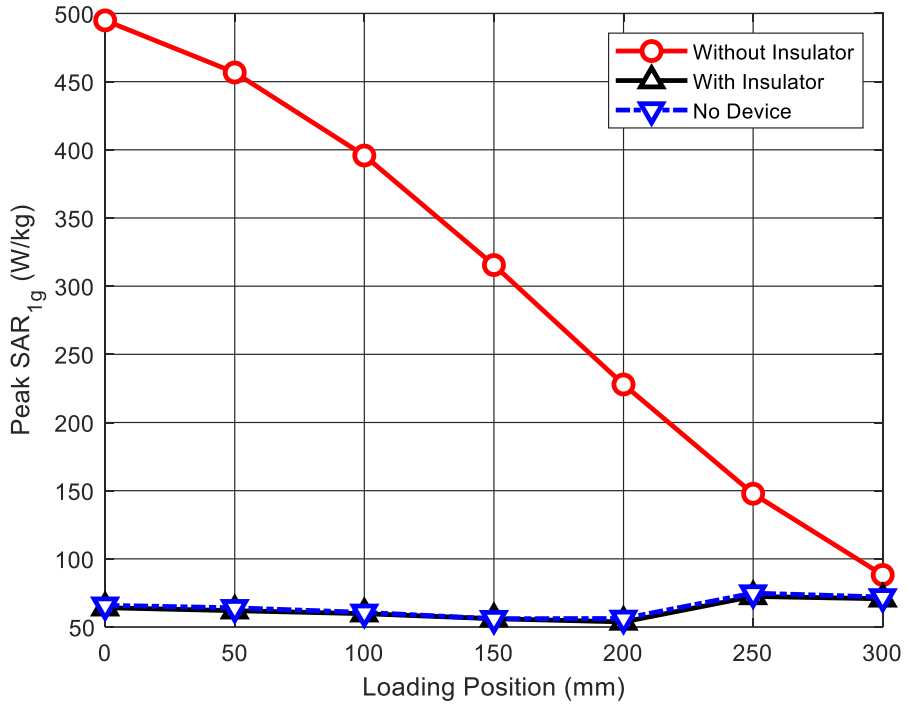

(b)

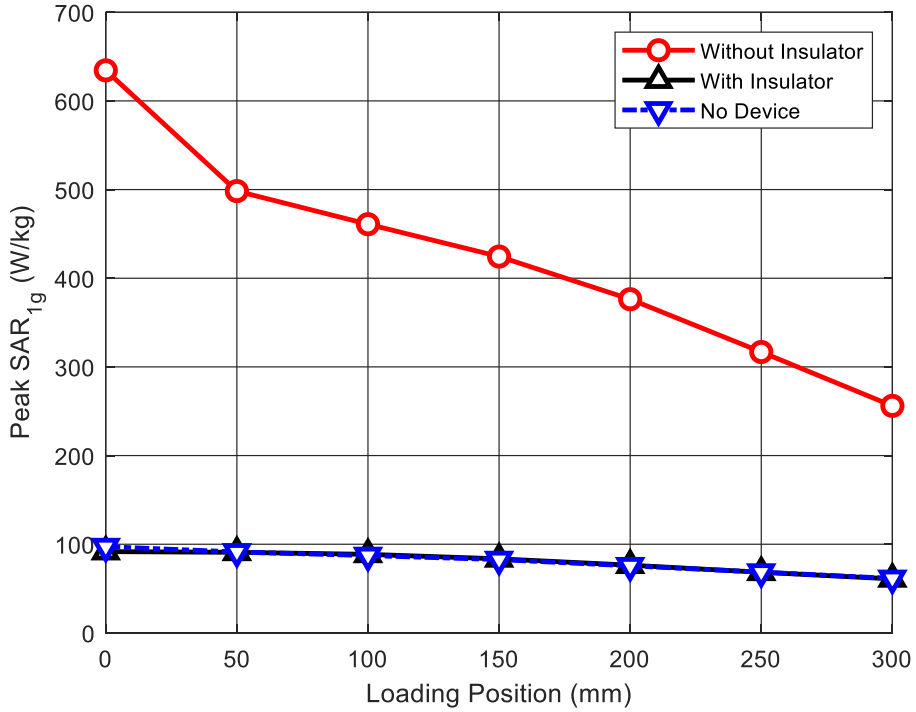

Figure 4-15. Peak local SAR_{1g} in the human model varied with the loading position.

4.5 Experimental Validation

To validate the effectiveness of the detuning strategy in a real clinical scenario, heating measurements were performed for the external fixation device with and without insulating covers in both 1.5 T and 3 T MRI coils. For the measurement setup, we built the ASTM phantom with the following dimensions: 420 mm × 180 mm × 650 mm. The ASTM phantom was filled with the gel made of sodium chloride (NaCl, 1.32 g/L) and polyacrylic acid (10 g/L) dissolved in water. The phantom was filled with the gel to a depth of 90 mm. The optical-fiber thermal probes were placed at the tips of the device pins. The total exposure time of the tested device in the RF field is 12 minutes at 1.5 T and six minutes at 3 T.

4.5.1 Tibia External Fixation

A commercially available tibia external fixator was used for testing through the experiments. As shown in Figure 4-16, both 1.5 T and 3 T MRI RF coils were used in the experiments. Optical-fiber thermal probes were used to measure the temperature rises near the pin tips. To hold the external fixation at the correct position, a wooden holder was used as shown in Figure 4-16 (c). Both rods and pins were covered with insulating layers as shown in Figure 4-16 (d). The insulating layer is made of polylactic acid (PLA), the dielectric constant of which is reported to be two to three. The thickness of the rod cover is 2 mm and the thickness of the pin cover is 1 mm. A thicker insulating layer was not used because it would make the mechanical structure of the tibia external fixation tested in the experiment unstable.

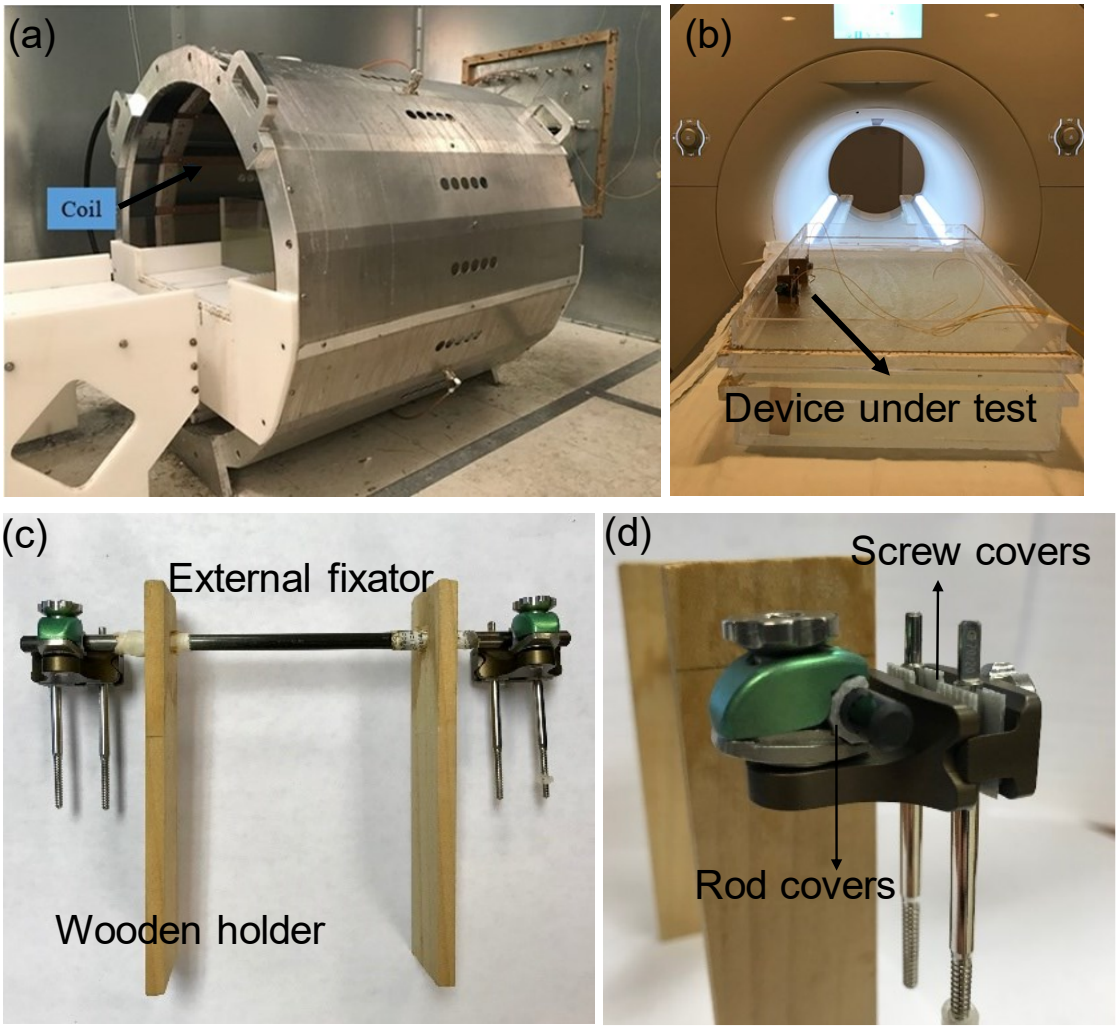

Figure 4-16. (a) A 1.5 T RF coil, (b) A 3 T MRI coil, (c) A commercial available external fixation device with wood holder, (d) Insulating materials applied on the rods (rod covers) and pins (pin covers).

Figure 4-17 shows the temperature rises of the external fixators with and without insulating covers in both 1.5 T and 3 T MRI. The temperature rise of the external fixation device is significantly reduced by applying insulating covers around the rods and pins. At 1.5 T, the temperature increase for the device without insulating covers is 7.85 °C, while it is only 1.01 °C for the device with insulating covers. A heating reduction of 87.13% is achieved by placing insulating materials in both clamp-rods joints and clamp-pin joints. The same effect is observed at 3 T. It is shown in Figure 4-17 (b) that the temperature rise

is reduced from 16.70 °C to 0.32 °C at 3 T. A heating reduction of 98.08% is achieved. Our experimental results demonstrate that the proposed detuning method can effectively reduce the heating of the external fixations at both 1.5 T and 3 T MRI. Furthermore, it also verifies the validity of the circuit model of the external fixation and indicates that increasing the total impedance of the external fixation is essential to the heating reduction in MRI.

A comparison between the simulated results and the experimental results is summarized in Table 4-3. Both results were obtained at 1.5 T. For the device without any capacitive structures, the absolute error between the simulation and the experiment is 2.76 °C and the relative error is 26.07%. For the device with pin covers and rod covers, the absolute error between the simulation and the experiment is 0.13 °C and the relative error is 11.40%. In general, these errors are within an acceptable range, which again validates the effectiveness of the strategy use of capacitive structures. The error analysis between experiments and simulations at 3 T is not performed in this study. This is because the RF field at 3 T was generated by a real MRI machine, the detailed structure of which is unknown to us. Moreover, the 3 T MRI machine will automatically perform RF shimming during the imaging process. We cannot model the equivalent RF environment in the simulations.

Table 4-3. Temperature rises of the tibia external fixation from simulations and experiments

	Simulated Results (°C)	Experimental Results (°C)
Without Insulator	10.61	7.85
With Insulator	1.14	1.01

(a)

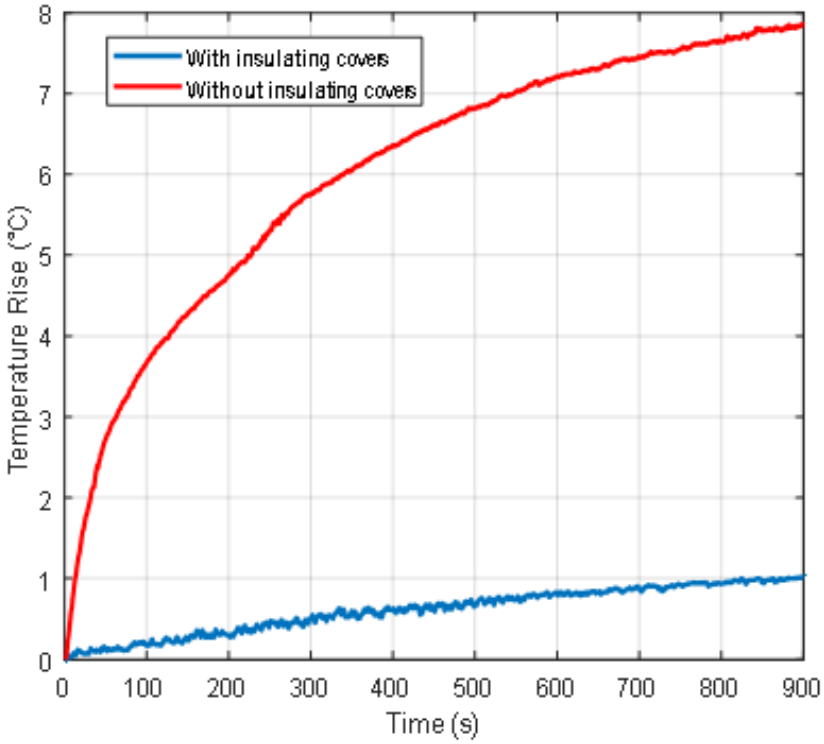

(b)

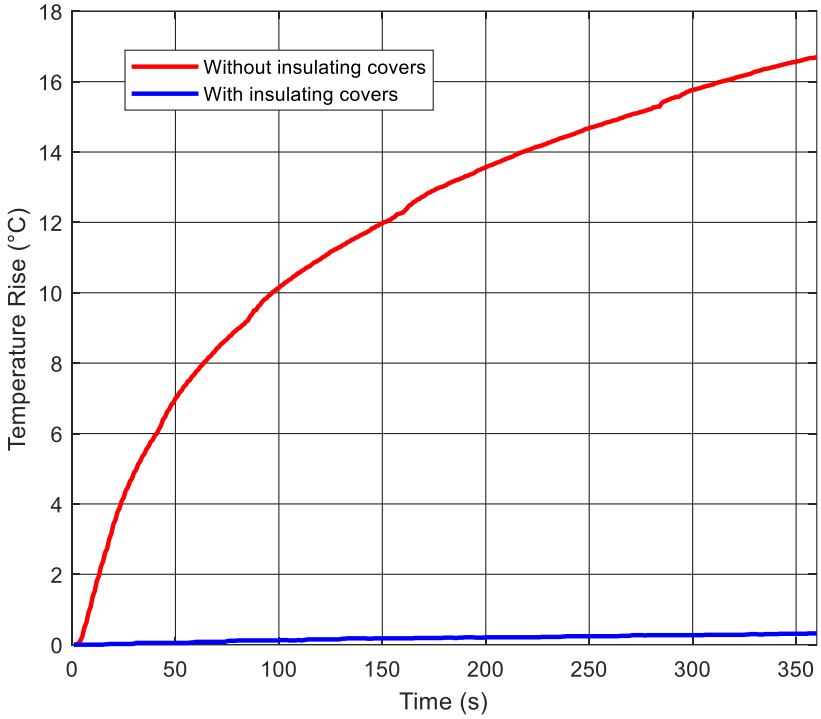

Figure 4-17. Temperature rise near the pin tip of external fixation device with and without insulating covers at (a) 1.5 T, and (b) 3 T.

4.5.2 Pelvic External Fixation

In addition to the tibia external fixation, a pelvic external fixation device was also used for testing in the experiments as shown in Figure 4-18. Only pin covers were applied to the device since there is no extra space for rod covers in this pelvic external fixation device. The thickness of the pin cover is 1 mm. A thicker insulating layer was not used because it would make the pelvic external fixation mechanically unstable.

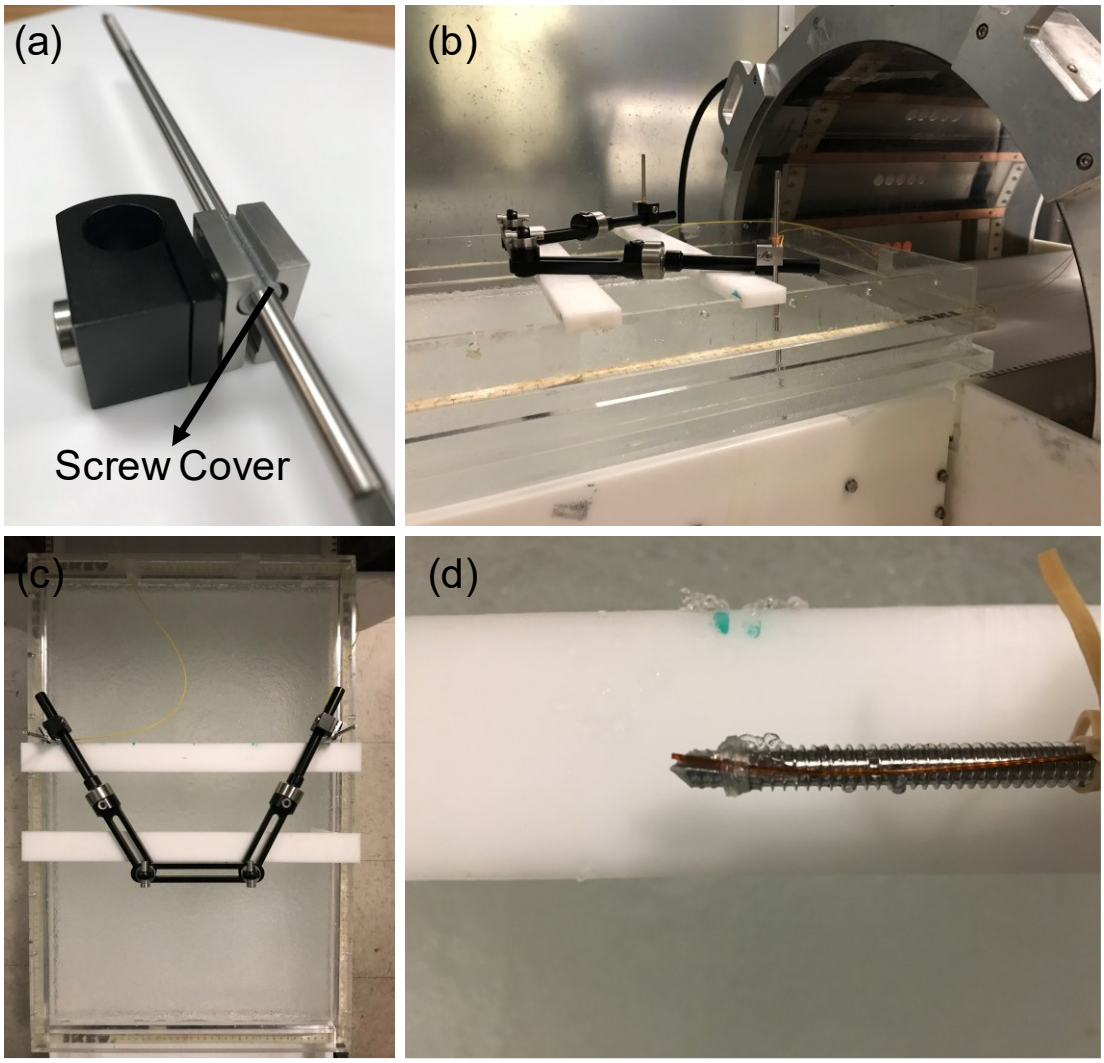

Figure 4-18. (a) Insulating material applied on the screw. (b) Pelvic external fixation and the 1.5 T RF coil. (c) Placement of the pelvic external fixation device. (d) A thermal probe attached to the screw tip.

The temperature rises at the pin tips of the pelvic device with and without insulating material are plotted in Figure 4-19. It is found that applying capacitive structures by insulating material can significantly reduce the RF-induced heating for the pelvic external device at 1.5 T.

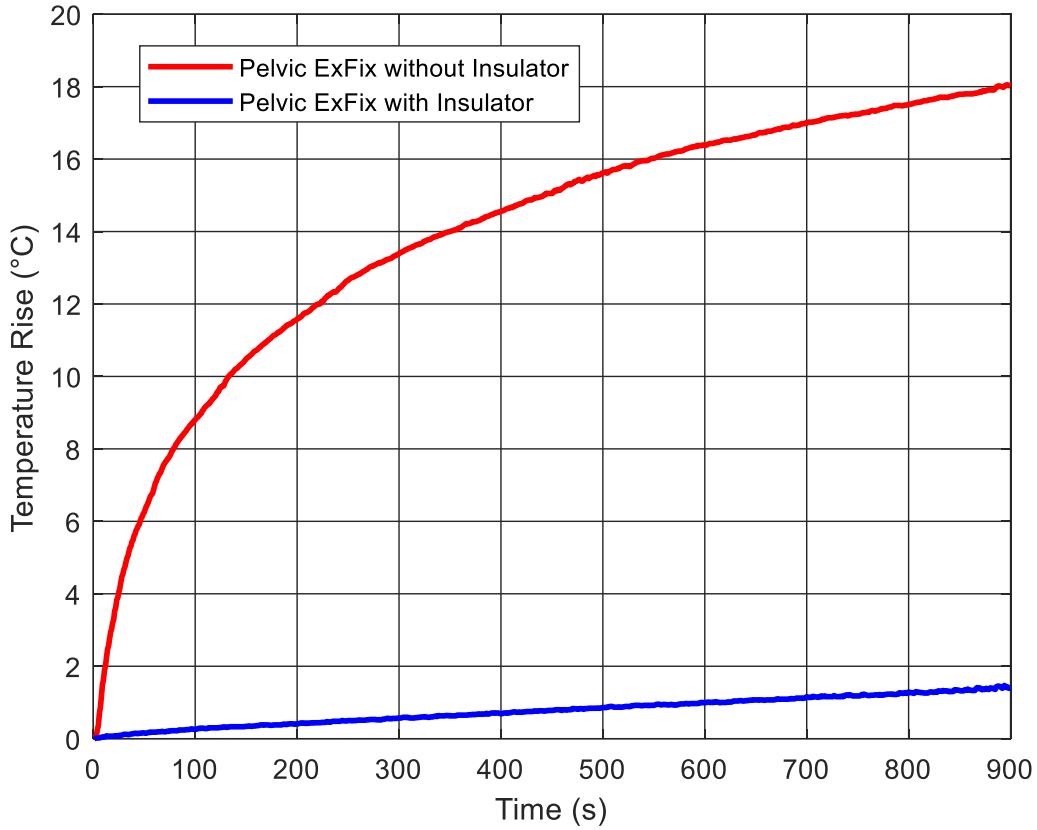

Figure 4-19. Temperature rise near the pin tip of the pelvic external fixation device with and without insulating covers at 1.5 T.

A comparison between the simulated results and the experimental results at 1.5 T is summarized in Table 4-4. For the case without any insulator, the absolute error between the simulation and the experiment is 1.54 °C and the relative error is 7.88%. For the case with pin covers, the absolute error between the simulation and the experiment is 0.37 °C and the relative error is 19.07%. In general, these errors are within an acceptable range, which also validates the effectiveness of the strategy use of capacitive structures.

Table 4-4. Temperature rises of the pelvic external fixation device from simulations and experiments

	Simulated Results (°C)	Experimental Results (°C)
Without Insulator	19.55	18.01
With Insulator	1.94	1.57

4.6 Discussion

Recent investigations have shown that insulating materials have the potentials to reduce the RF-induced heating of external fixations. However, most studies focus on the effects of insulating materials at 1.5 T MRI rather than high field MRI. Moreover, the fundamental mechanism of the insulating materials in reducing the RF-induced heating fails to be illustrated completely and thoroughly. In this paper, we used the numerical calculations and experiments to investigate the mechanism of the heating reduction by using insulating materials at both 1.5 T and 3 T. It is found that inserting insulating material in the joints of the pins and clamps can effectively reduce the RF-induced heating for external fixations at 1.5 T. Also, decreasing the dielectric constant and increasing the thickness of the insulating materials can further reduce the heating at 1.5 T. However, this method cannot mitigate the RF-induced heating at 3 T. In the specific case, placing insulating material with low relative permittivity in the clamp-pin joints will even aggravate the RF-induced heating at 3 T. This finding indicates that heuristically or intuitively applying pin covers is not guaranteed to reduce RF-induced heating of external fixation devices, carefully design procedure is needed to detune the coupling between the external fixation device and the RF field.

To explain the heating mechanism of the external fixations, we built an equivalent circuit model. According to the model, the external fixation device can be regarded as an RF voltage source connected with a lumped inductor. The effects of the power dissipation

near the pin tip can be modeled as a resistive load. The RF-induced heating results from the RF power dissipated by the tissue. At 1.5 T, when we apply insulating covers with low relative permittivity on the pins, the overall impedance of the device will become capacitive. As the relative permittivity of the material decreases and the thickness of the covers increases, the capacitive impedance of the device will increase. Subsequently, the current flowing on the device is decreased. As a result, the dissipated power near the tip is reduced as well as the heating effect.

By comparison, at 3 T MRI, the external fixation device will resonant as the capacitive reactance introduced by the pin covers cancels the inductive reactance of the device. The resonant condition of an RLC circuit is $\omega^2 LC = 1$. For a specific external fixation device, the inductance of the device is fixed. As the MRI frequency increases to 128 MHz at 3 T, the capacitance required to make the circuit resonant will decrease. Therefore, either reducing the relative permittivity of the insulating material or increasing its thickness will reduce the capacitance and cause the device resonant. Once the resonance occurs, the currents on the device and the dissipated power near the pin tips will become extremely large and the worst-case heating will occur.

To avoid the worst-case RF-induced heating and further reduce this heating, detuning the resonant circuit and increasing the equivalent impedance of the external fixation is necessary. In this study, introducing extra capacitive structures to the external fixation device was applied. By placing extra insulating materials in the joints of the rods and clamps, the equivalent circuit of the external fixation is detuned, and the impedance of the device is increased. It is found from the simulated results that by placing insulating materials in both clamp-rod joints and clamp-pin joints, the RF-induced heating is

reduced 98.35% at 1.5 T and 95.24% at 3 T on average. Moreover, the experiments were performed to validate the simulations. Heating measurements show that the temperature rises near the pin tip are reduced from 7.85 °C to 1.01 °C for 1.5 T and 16.70 °C to 0.32 °C for 3 T. Both simulated results and experimental results demonstrate that detuning the equivalent circuit of the external fixation device and further increasing the device impedance effectively mitigate the RF-induced heating at both 1.5 T and 3 T.

It is worth noting that applying capacitive structures to external fixation devices cannot eliminate the artifacts resulting from the metallic medical devices. Therefore, it is not suitable to use MR to image tissues with the external fixation device, even if the device is modified with capacitive structures. However, the strategy of applying capacitive structures will still be helpful when the patient with the tibia external fixation device requires a torso scan or a brain scan under MRI. This application enlarges the safety margin for patients with external fixation devices undergoing MRI.

4.7 Conclusion

In this study, we proposed a promising method to reduce the RF-induced heating of the external fixation at both 1.5 T and 3 T MRI. An equivalent circuit was built to illustrate the heating effect of external fixation devices under the MR scan. It is concluded from the circuit model that increasing the equivalent impedance of the external fixation device can reduce the RF-induced heating for the external fixation device. Furthermore, it is found that the RF-induced heating will become extremely severe at 3 T MRI when the external fixation device simply has insulating material covered in the joints of the pins and the clamps. This is because that the capacitive reactance introduced by the pin covers exactly cancels the inductive reactance of the device at 3 T. By

applying insulating materials on both rods and pins, we successfully detuned the equivalent circuit of the external fixation and increased the total impedance of the device. Both simulated results and experimental results show that the RF-induced heating of the external fixation is reduced using this method. In future investigations, it is necessary to validate the effectiveness of the detuning strategy for various external fixation types and different MRI frequencies.

Chapter 5

Numerical Investigation of RF-induced Heating in Birdcage and TEM Body Coils

5.1 Background

Recently, transverse electromagnetic (TEM) coil has been demonstrated as a promising alternative to birdcage (BC) coil for magnetic resonance imaging (MRI) at high strength magnetic fields. Both numerical and experimental investigations have shown that the TEM coil possesses better magnetic field homogeneity and higher signal-noise-ratio (SNR) over the BC coil in the loaded cases [61], [62]. Moreover, compared with BC coil, the resonant elements of TEM coil are separate and directly connected to the metal shield, which ensures that the resonance of the TEM coil is independent of the diameter of the coil [63]. Thus, TEM coils with various diameters can be built to satisfy diverse clinical requirements.

In 2006, Wang and Shen compared the performance of birdcage, TEM and microstrip volume coils at 7 T. They found that the birdcage coil has the best unloaded B1 homogeneity and the TEM coil has the best loaded B1 field homogeneity and the lowest radiation loss [64], while the microstrip coil is better in the average SNA at 7 T. This study mainly investigated the imaging performance of the different RF coil types, while showed little attention on the RF-induced heating effect. Later in 2011, Yeo et al. studied the effects of different RF coil designs on the peak local specific absorption rate (SAR) in multiple human body models at 3 T MRI [65]. They found that the local SAR distributions in human models were highly variable and the impact of the coil types on

the peak local SAR values is not statistically significant. This study only considered the overall RF energy absorbed by the human body and ignored the heating effect in the presence of implanted medical devices. As the heating effects caused by the medical implants are stronger and more likely to cause severe thermal damage to the human body, it is essential to investigate the heating effect in the human body and phantom with medical devices [66]. In literature, BC coil is commonly used to study the RF-induced heating of the medical device. Since the TEM coil employs independent transmission lines to generate the RF field propagating in TEM mode, the heating effect in the TEM coil will be quite different from that of the BC coil. Although there are preliminary studies that comparing the local SAR between TEM and BC coils in the presence of an implanted pacemaker [67], they failed to explain the reason why TEM coil will generate different heating effects from BC coil. Moreover, they only considered a simple implanted wire and ignored the passive devices. Considering the emerging use of the TEM coil for a high strength MRI system, it is essential to evaluate the RF-induced heating effect resulting from the TEM coil in the presence of medical implants.

In this paper, we numerically calculate the incident electromagnetic fields in TEM and BC coils. The peak local SAR values inside the standard phantom with the implanted device were assessed for both TEM and BC coils. Two common medical implants were considered, namely orthopedic plates and spinal fixations. The impact of the length of the implanted device was investigated. It is found that the worst-case length that causes the maximum peak local SAR is 10.0 cm for both BC and TEM coils. Moreover, for both orthopedic plates and spinal fixations, BC coil generates larger RF-induced heating in the standard phantom compared with the TEM coil. According to the incident electric field

results, this is because the magnitude of the z-direction electric field in the BC coil is stronger than it is in the TEM coil.

5.2 TEM and BC Body Coils

SEMCAD X (V14.8, SPEAG, Zurich, Switzerland), a commercial full-wave electromagnetic field solver based on the finite-difference time-domain (FDTD) method, is used to compute the incident electromagnetic field distributions. The study was done at 128 MHz, which is the Larmor frequency of 3 T MRI system.

To simulate the RF field in the MRI system, two RF body coils were built, namely BC coil and TEM coil. As shown in Figure 5-1, both coils are modeled using 16 perfect electric conductor (PEC) rungs, each of which has a width of 20 mm and a length of 450 mm. Both coils have a diameter of 620 mm.

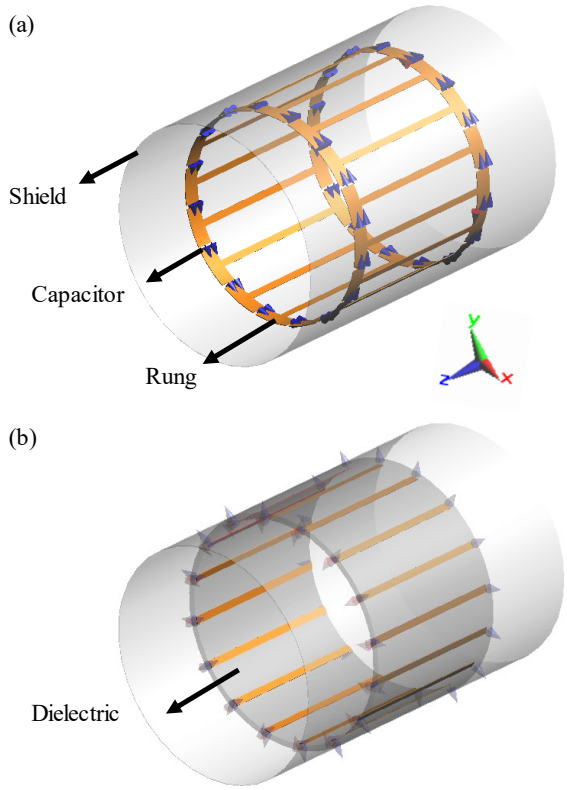

Figure 5-1. Models of the designed RF body coils: (a) Birdcage coil, (b) TEM coil.

For the TEM coil, all the 16 rungs are connected to a PEC shield through 32 terminal capacitors. The dielectric between the PEC rungs and the PEC shield has a thickness of 20 mm and a relative permittivity of 2. To ensure the TEM coil operates at a resonant frequency of 128 MHz, all the terminal capacitors (CT) are tuned to be 13.3 pF. A capacitor (CM) of 5.5 pF was serially connected to each resonant element to match the input impedance of 50 Ω. Figure 5-2 shows the detailed structure of a single resonant element connecting to the voltage source. The design procedure of the TEM coil can be found in [68]. For the BC coil, 64 capacitors of 9.4 pF on the two end rings are used to make the coil resonant at 128 MHz. The width of the end ring is 50 mm. The tuning process of the BC coil can be found in [63]. Both coils are excited in the quadrature mode and are placed in a PEC shield with a length of and 1000 mm and a diameter of 700 mm. In this study, the bore direction of the coil is denoted as the z-axis and the transverse plane is represented by the XY-plane.

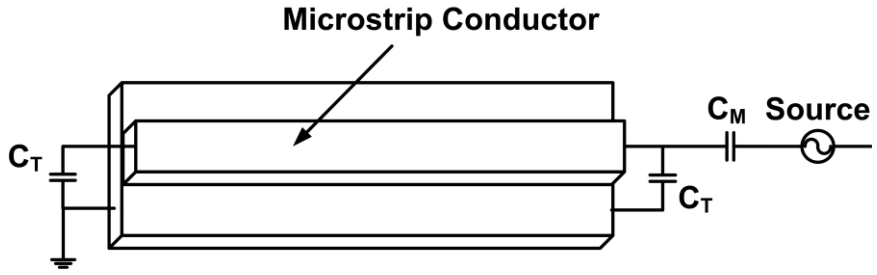

Figure 5-2. Single resonant element of the designed TEM coil. CT denotes the tuning capacitor and CM denotes the matching capacitor.

5.3 Orthopedic Plate and Spinal Fixation

Without loss of generality, an orthopedic plate and a spinal fixation were built in this study. As shown in Figure 5-3, the orthopedic device was modeled using one PEC

plate and two PEC screws. The orthopedic plate has a thickness of 5 mm and a width of 10 mm. The orthopedic screw has a length of 32 mm and a diameter of 9 mm. As shown in Figure 5-3 (b), the spinal fixation was modeled using one PEC rod and two PEC screws. The spinal rod has a diameter of 3.5 mm. The spinal screw has a length of 32 mm and a diameter of 3.5 mm. In the initial setting, the plate length and the rod length are set to be 50 mm. Then the length variations including 50 mm, 75 mm, 100 mm, 125 mm, and 150 mm were investigated.

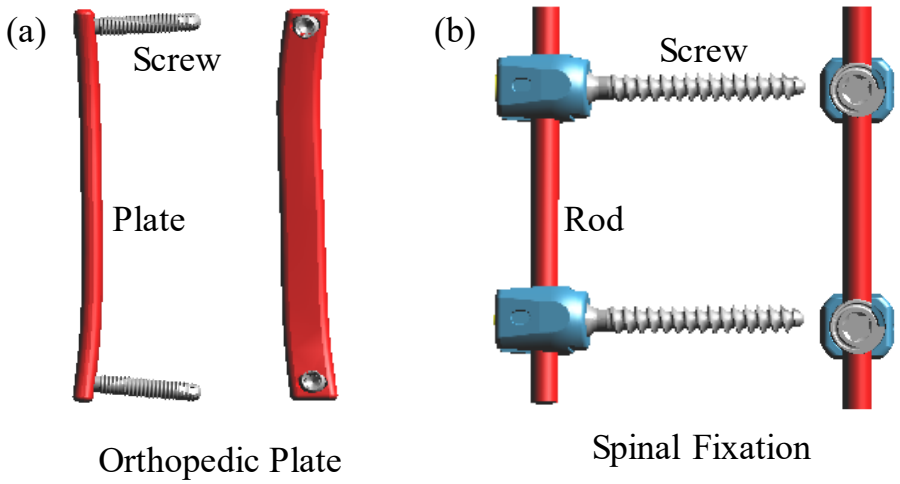

Figure 5-3. Generic models of (a) an orthopedic plate, and (b) a spinal fixation.

5.4 RF Field Comparison

For unloaded TEM and BC coils, the patterns of the incident magnetic field are obtained for an input power of 1 W. Both patterns are extracted at the center plane ($z = 0$) and plotted in Figure 5-4 using the root mean square (RMS) values. As we can see, for both BC coil and TEM coil, the magnetic fields are uniformly distributed within the coils. The good homogeneity of the magnetic field distribution indicates that the RF coils are operating at the correct resonant mode.

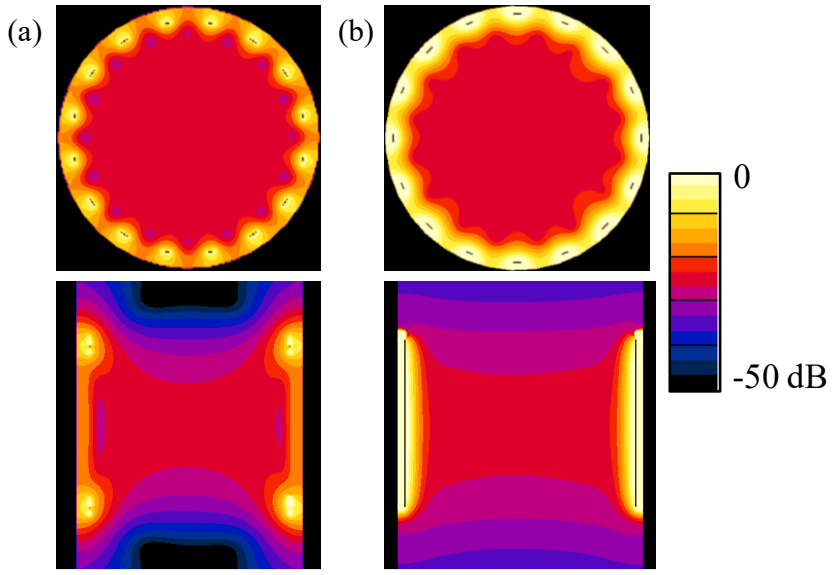

Figure 5-4. Magnitude distribution of B field in unloaded (a) BC coil and (b) TEM coil. The first row is the axial plane and the second row is the sagittal plane. 0 dB corresponds to 5 µT.

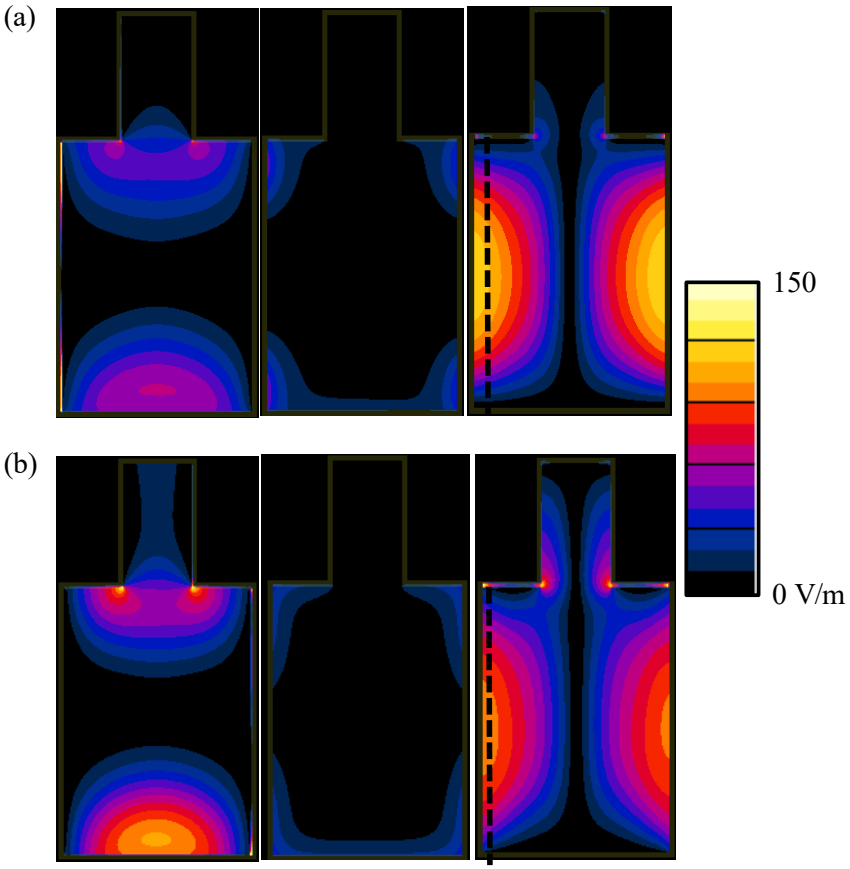

Figure 5-5. Magnitude distribution of RMS electric field in the ASTM phantom for (a) BC coil and (b) TEM coil. The first column to the third column corresponds to the x-component, y-component, and z-component of the incident electric field.

Figure 5-5 shows the magnitude distributions of the RMS electric field ($\|E_{RMS}\|$) in BC coil and TEM coil, when the ASTM phantoms are loaded inside the coils. For a meaningful comparison, the input power was set to obtain a whole-body SAR of 2 W/kg in the ASTM phantom. As shown in Figure 5-5, for both BC and TEM coils, the electric field in the phantom is primarily along the z-direction. To further compare the electric fields of the BC coil and TEM coil, the magnitude of the $\|E_{RMS}\|$ along the z-axis which is 2 cm from the phantom sidewall (the black dash line in Figure 5-5) is extracted and plotted in Figure 5-6. As we can see, $\|E_{RMS}\|$ of BC coil in the middle part of the phantom is larger, compared with TEM coil. Moreover, in the phantom bottom, $\|E_{RMS}\|$ of TEM coil is larger than that of BC coil. This different distribution of incident electric field between TEM and BC coils will lead to distinct RF-induced heating effects in the phantom with passive implants.

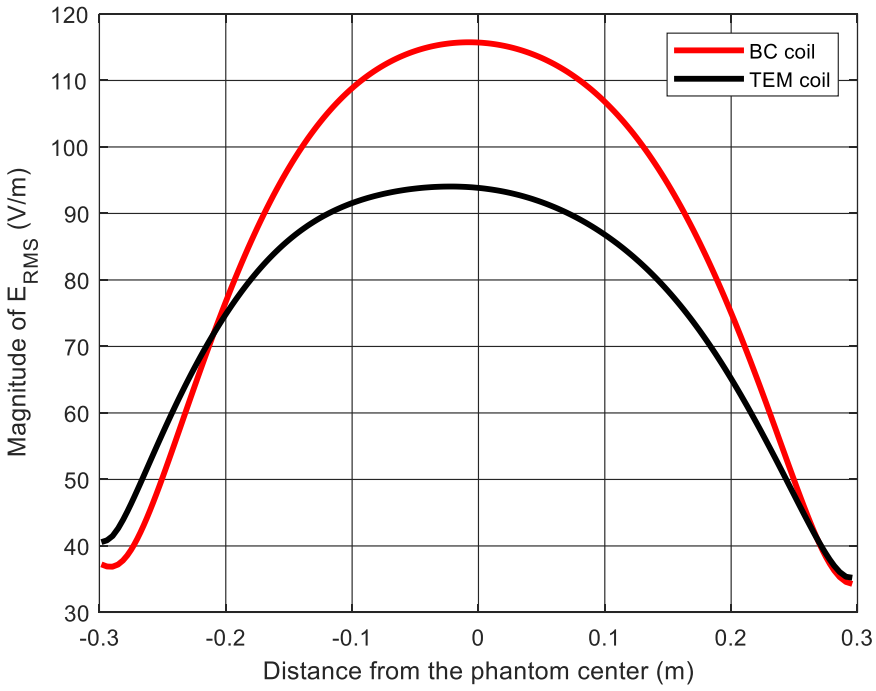

Figure 5-6. Magnitude of RMS electric field along the z-axis that is 2 cm from the phantom sidewall.

5.5 Heating Comparison

The peak local SAR averaged over 1 g (SAR1g) in the ASTM phantom is utilized to represent the RF-induced heating. Figure 5-7 and Figure 5-8 show how the peak local SAR_{1g} varies with the device length in BC and TEM coils. For both coils, as the device length increases the peak local SAR_{1g} in the ASTM phantom rises first and then decreases. Moreover, the device length that causes the worst heating result is 10.0 cm for both BC and TEM coils. This result can be explained by the antenna theory. As the RF fields in both coils are resonant at 128 MHz, the device that is closer to the half wavelength in the ASTM phantom tends to receive larger RF energy. This larger RF energy eventually results in a larger local peak SAR_{1g} in the ASTM phantom.

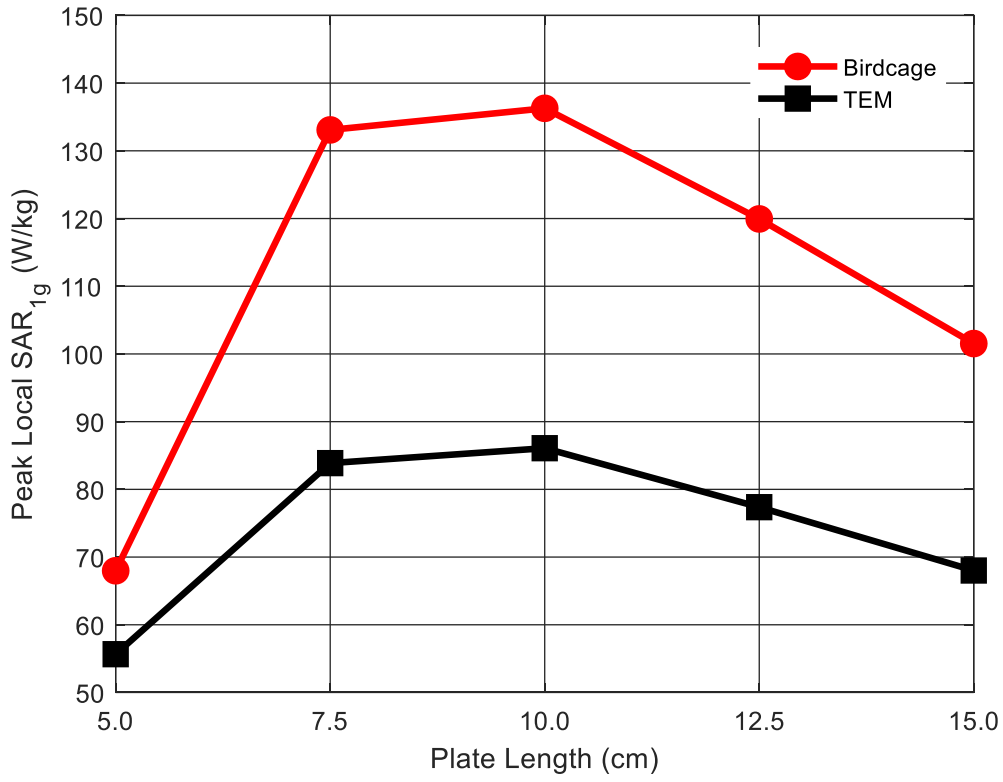

Figure 5-7. Peak local SAR_{1g} in the ASTM phantom with the orthopedic plate.

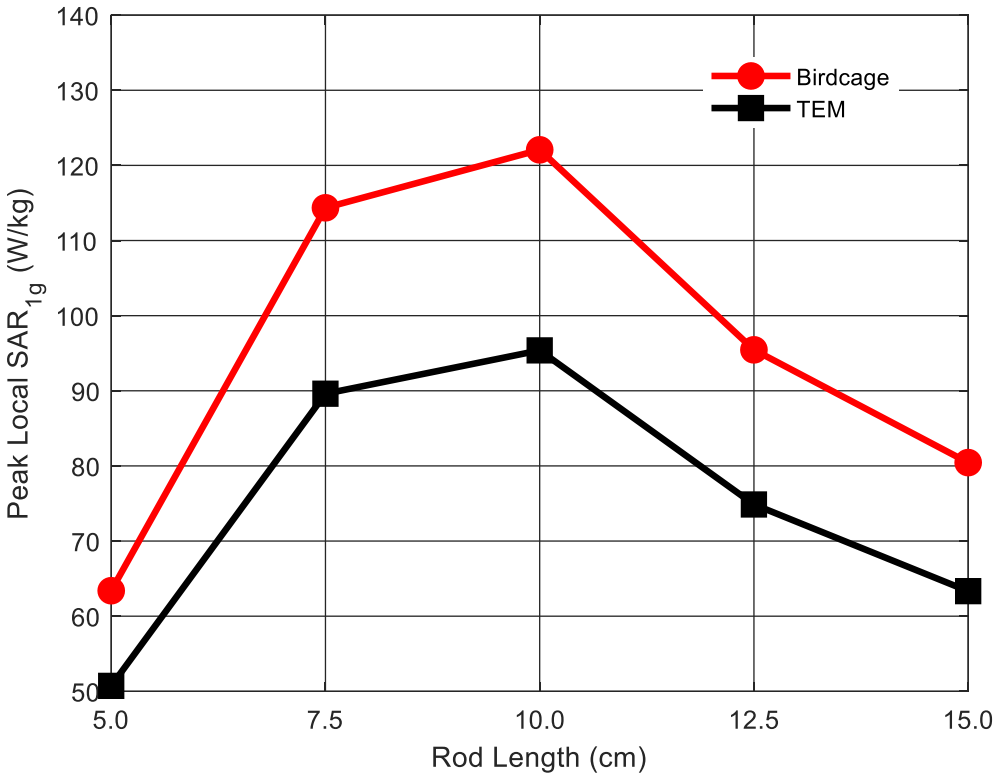

Figure 5-8. Peak local SAR1g in the ASTM phantom with the spinal fixation.

In addition to the worst-case length, it is also found that the peak local SAR_{1g} in the ASTM phantom in the BC coil is larger than it is in the TEM coil. It is known that the BC coil produces a stronger z-directional electric field in the ASTM phantom, compared with the TEM coil. Since the orthopedic plate and spinal fixation are mainly along the z-direction, they tend to receive more RF energy in the BC coil than the TEM coil. This fact indicates that the BC coil tends to cause larger RF-induced heating than the TEM coil does in the presence of z-orientated passive implants. Also, it would be more conservative to use BC coil, rather than TEM coil, to evaluate the RF-induced heating of medical implants.

5.6 Summary

In this paper, two different RF body coils, namely BC coil and TEM coil, have been built. Electromagnetic simulations were performed in the ASTM phantom with orthopedic plates and spinal fixations for both coils. We find that the magnitude of the z-component of the electric field in the BC coil is larger than it in TEM coil. Due to this fact, BC coil generates a higher heating level in ASTM phantom than BC coil in the presence of passive implants with large dimensions along the coil bore, such as orthopedic plates and spinal fixations. This result also indicates that in the presence of passive implants, patients undergoing TEM coil will be safer than those undergoing BC coil. Also, BC would be more conservative than the TEM coil for evaluating the RF-induced heating of medical implants. In the future, further investigations concerning the heating mechanism of TEM coils will be needed before applying them to clinical diagnosis.

Chapter 6

Conclusions and Future Work

6.1 Conclusions

Patients with medical implants requiring MRI scan is constantly growing. However, patients with implants are either exempted from MRI scans or scanned with very conservative RF power limitations due to the potential safety hazards. One of the primary safety concerns is the tissue heating caused by the coupling between the RF field and the metallic implant. In particular, tissue heating can be very localized, causing permanent damage to human tissue. Therefore, it is essential to develop effective techniques to mitigate the RF-induced heating in the presence of medical implants. In this dissertation, three methods are proposed to reduce the RF-induced heating of various medical devices. Both simulations and experiments are performed to demonstrate the effectiveness of the proposed methods.

For the implantable lead, it was proposed to reduce the RF-induced heating by modifying the electrode design. We found that enlarging the electrode contact could reduce the temperature rise at the lead electrode. By increasing the electrode to a 270° circle, the simulation results show a temperature reduction of 31.25% near the electrode edge and 26.06% at the lead tip, and the experimental results show a reduction of 27.49% at the lead tip. This is because the increased contact area between the lead electrode and phantom gel reduces the decreased energy deposition density.

For the external fixation, the effects of insulating material on RF-induced heating for external fixation was investigated in 1.5 T and 3 T MRI by both numerical calculation

and experiments. It was found that inserting a thin low relative permittivity insulation between the pins and clamps could effectively reduce the heating in 1.5 T MRI, while it would fail in 3 T MRI. What is worse, this method would even aggravate the RF-induced heating at 3 T due to the resonant effect. The key to the RF heating reduction is to increase the total impedance of the external fixation. Carefully designed capacitive structures, which introduce enough capacitive reactance to the external fixation, were utilized to reduce the RF-induced heating.

For the passive implants, we investigated the effects of the transverse electromagnetic (TEM) coil and the birdcage (BC) coil on the RF-induced heating. Electromagnetic simulation results indicate that the BC coil generates a stronger incident electric field along the coil bore than the TEM coil does. Due to this reason, BC coil generates a higher heating level in ASTM phantom than TEM coil in the presence of passive implants with large dimensions along the coil bore, such as orthopedic plates and spinal fixations.

6.2 Future Works

In this dissertation, three methods have been proposed and investigated to reduce the RF-induced heating of medical implants. Both simulations and experiments have been performed to demonstrate the effectiveness of these methods. However, there are still many issues to consider before putting the techniques into practice.

First, the effect of the electrode modification on the performance of the lead and the associated stimulating system needs further investigation. This is because the change in the electrode structure may affect the stimulating voltage at the electrode. Moreover, it

is also important to study the effect of the electrode modification on RF-induced heating for multi-electrode leads.

Second, the strategy of using capacitive structures was only explored in 1.5 T and 3 T MRI. For practical implementations, it would be more useful to shift the resonance frequency towards even higher frequencies by implementing more capacitive structures. This would allow for a field strengths independent solution that suppresses the RF heating and makes the external fixation devices safe at all clinical field strengths.

Last, it is necessary to validate the RF-induced heating of the TEM coil experimentally in the standard phantom with realistic devices. This is because the less heating benefiting from the use of TEM coil is only predicted with numerical simulations in this dissertation. Also, it is important to compare the RF-induced heating between the TEM coil and the BC coil in the presence of other medical implants, such as active implantable leads and external fixation devices. These devices have different structures and locations in the human body.

References

[1] F. C. Shellock and J. V. Crues, “MR procedures: biologic effects, safety, and patient care,” *Radiology*, vol. 232, no. 3, pp. 635–652, 2004.

[2] Y. Liu, J. Chen, F. G. Shellock, and W. Kainz, “Computational and experimental studies of an orthopedic implant: MRI-related heating at 1.5-T/64-MHz and 3-T/128-MHz,” *Journal of Magnetic Resonance Imaging*, vol. 37, no. 2, pp. 491–497, 2013.

[3] J. Zheng, D. Li, J. Chen, and W. Kainz, “Numerical study of SAR for multi-component orthopaedic hip replacement system during MRI,” *IEEE International Symposium on Electromagnetic Compatibility*, 2016, pp. 116–120.

[4] J. Powell, A. Papadaki, J. Hand, A. Hart, and D. McRobbie, “Numerical simulation of SAR induced around Co-Cr-Mo hip prostheses in situ exposed to RF fields associated with 1.5 and 3 T MRI body coils,” *Magnetic Resonance in Medicine*, vol. 68, no. 3, pp. 960–968, 2012.

[5] L. Winter, E. Oberacker, C. Özerdem, Y. Ji, F. Von Knobelsdorff-Brenkenhoff, G. Weidemann, B. Ittermann, F. Seifert, and T. Niendorf, “On the RF heating of coronary stents at 7.0 Tesla MRI,” *Magnetic Resonance in Medicine*, vol. 74, no. 4, pp. 999–1010, 2015.

[6] X. Ji, J. Zheng, and J. Chen, “Numerical evaluation of RF-induced heating for gap and pitch variation of helical stent under MRI,” in *2017 IEEE Antennas and Propagation Society International Symposium, Proceedings*, 2017 January, pp. 1017–1018.

[7] D. Li, X. Ji, J. Zheng, C. Pan, J. Chen, and W. Kainz, “A novel design of

implantable esophageal stent to reduce the MRI RF-induced heating," *IEEE Transactions on Electromagnetic Compatibility*, vol. 59, no. 3, pp. 805–812, 2017.

[8] X. Ji, J. Zheng, R. Yang, W. Kainz, and J. Chen, "Evaluations of the MRI RF-induced heating for helical stents under a 1.5T MRI System," *IEEE Transactions on Electromagnetic Compatibility*, vol. 61, no. 1, pp. 57–64, 2019.

[9] R. Luechinger, P. Boesiger, and J. A. Disegi, "Safety evaluation of large external fixation clamps and frames in a magnetic resonance environment," *Journal of Biomedical Materials Research Part B: Applied Biomaterials*, vol. 82, no. 1, pp. 17–22, 2006.

[10] Y. Liu, J. Shen, W. Kainz, S. Qian, W. Wu, and J. Chen, "Computational study of external fixation devices surface heating in MRI RF environment," in *IEEE International Symposium on Electromagnetic Compatibility*, 2012, pp. 612–616.

[11] Y. Liu, J. Shen, W. Kainz, S. Qian, W. Wu, and J. Chen, "Numerical investigations of MRI RF field induced heating for external fixation devices," *BioMedical Engineering Online*, vol. 12, no. 1, pp. 1–14, 2013.

[12] R. Tanaka, T. Yumoto, N. Shiba, M. Okawa, T. Yasuhara, T. Ichikawa, K. Tokunaga, I. Date, and Y. Ujike, "Overheated and melted intracranial pressure transducer as cause of thermal brain injury during magnetic resonance imaging: case report," *Journal of Neurosurgery*, vol. 117, no. 6, pp. 1100–1109, 2012.

[13] B. L, I. C, K. BH, and T. D, "Third degree skin burns caused by a MRI conditional electrocardiographic monitoring system," *Journal of Radiology and Imaging*, vol. 1, no. 4, pp. 29–32, 2016.

[14] C. J. Yeung, R. C. Susil, and E. Atalar, "RF heating due to conductive wires

during MRI depends on the phase distribution of the transmit field," *Magnetic Resonance in Medicine*, vol. 48, no. 6, pp. 1096–1098, 2002.

[15] C. J. Yeung, R. C. Susil, and E. Atalar, "RF safety of wires in interventional MRI: Using a safety index," *Magnetic Resonance in Medicine*, vol. 47, no. 1, pp. 187–193, 2002.

[16] G. Calcagnini, M. Triventi, F. Censi, E. Mattei, P. Bartolini, W. Kainz, and H. I. Bassen, "In vitro investigation of pacemaker lead heating induced by magnetic resonance imaging: role of implant geometry," *Journal of Magnetic Resonance Imaging*, vol. 28, no. 4, pp. 879–886, 2008.

[17] Q. Zeng, Q. Wang, J. Zheng, W. Kainz, and J. Chen, "Evaluation of MRI RF electromagnetic field induced heating near leads of cochlear implants," *Physics in Medicine and Biology*, vol. 63, no. 13, 2018.

[18] V. Acikel, B. Silemek, and E. Atalar, "Wireless control of induced radiofrequency currents in active implantable medical devices during MRI," *Magnetic Resonance in Medicine*, vol. 83, no. 6, pp. 2370-2381, 2020.

[19] J. Liu, D. R. Jackson, Q. Wang, W. Kainz, and J. Chen, "On the relationship between impedances of active implantable medical devices and device safety under MRI RF emission," *IEEE Transactions on Electromagnetic Compatibility*, pp. 1–9, 2019.

[20] V. Acikel, A. Uslubas, and E. Atalar, "Modeling of electrodes and implantable pulse generator cases for the analysis of implant tip heating under MR imaging," *Medical Physics*, vol. 42, no. 7, pp. 3922–3931, 2015.

[21] J. Liu, J. Zheng, Q. Wang, W. Kainz, and J. Chen, "A transmission line model for

the evaluation of MRI RF-Induced fields on active implantable medical devices," *IEEE Transactions on Microwave Theory and Techniques*, vol. 66, no. 9, pp. 4271–4281, 2018.

[22] S. M. Park, R. Kamondetdacha, and J. A. Nyenhuis, "Calculation of MRI-induced heating of an implanted medical lead wire with an electric field transfer function," *Journal of Magnetic Resonance Imaging*, vol. 26, no. 5, pp. 1278–1285, 2007.

[23] S. Feng, R. Qiang, W. Kainz, and J. Chen, "A technique to evaluate MRI-induced electric fields at the ends of practical implanted lead," *IEEE Transactions on Microwave Theory and Techniques*, vol. 63, no. 1, pp. 305–313, 2015.

[24] R. Yang, J. Zheng, Y. Wang, R. Guo, W. Kainz, and J. Chen, "An absorbing radio frequency shield to reduce RF heating induced by deep brain stimulator during 1.5-T MRI," *IEEE Transactions on Electromagnetic Compatibility*, vol. 61, no. 6, pp. 1726–1732, 2019.

[25] Food and Drug Administration, *Guidance For Industry And Food And Drug Administration Staff - Criteria For Significant Risk Investigations Of Magnetic Resonance Diagnostic Devices*. 2008.

[26] International Electrotechnical Commission, *Medical Electrical Equipment - Part 2-33: Particular Requirements For The Basic Safety And Essential Performance Of Magnetic Resonance Equipment For Medical Diagnosis*. IEC 60601-2-33, 2010.

[27] F. G. Shellock, T. O. Woods, and J. V. Crues, "MR labeling information for implants and devices: explanation of terminology," *Radiology*, vol. 253, no. 1, pp. 26–30, 2009.

[28] *Standard Test Method For Measurement Of Radio Frequency Induced Heating On Or Near Passive Implants During Magnetic Resonance*. ASTM F2182-11a, 2014.

[29] *Assessment Of The Safety Of Magnetic Resonance Imaging For Patients With An Active Implantable Medical Device*. ISO/TS 10974, 2012.

[30] D. J. Griffiths, "Quantum mechanics in three-dimension," in *Introduction to Quantum Mechanics*, Upper Saddle River: Prentice Hall, 1995, pp. 121–176.

[31] M. S. Brown and R. C. Semelka, "Concept of magnetic resonance," in *MRI: Basic Principles and Applications*, 3rd ed., Hoboken: John Wiley & Sons, 2004, pp. 11–20.

[32] H. H. Pennes, "Analysis of tissue and arterial blood temperatures in the resting human forearm," *Journal of Applied Physiology*, vol. 1, no. 2, pp. 93–122, 1948.

[33] F. G. Shellock, D. J. Schaefer, and E. Kanal, "Physiologic responses to MR imaging performed at an SAR level of 6.0 W/kg," *Radiology*, vol. 192, no. 3, pp. 865–868, 1994.

[34] F. G. Shelloc and D. J. Schaefer, "Radiofrequency energy-induced heating during MR procedures: a Review," *Journal of Magnetic Resonance Imaging*, vol. 12, no. 1, pp. 30–36, 2000.

[35] Y. Liu, W. Kainz, S. Qian, W. Wu, and J. Chen, "Effect of insulating layer material on RF-induced heating for external fixation system in 1.5 T MRI system," *Electromagnetic Biology and Medicine*, vol. 33, no. 3, pp. 223–227, 2014.

[36] J. Jin, *Electromagnetic Analysis And Design In Magnetic Resonance Imaging*, 1st ed. Boca Raton: CRC Press, 1998.

[37] A. Christ, W. Kainz, E. G. Hahn, K. Honegger, M. Zefferer, E. Neufeld, W.

Rascher, R. Janka, W. Bautz, J. Chen, B. Kiefer, P. Schmitt, H. P. Hollenbach, J. Shen, M. Oberle, D. Szczerba, A. Kam, J. W. Guag, and N. Kuster, "The virtual family development of surface-based anatomical models of two adults and two children for dosimetric simulations," *Physics in Medicine and Biology*, vol. 55, no. 2, 2010.

[38] J. E. Brown, R. Qiang, P. J. Stadnik, L. J. Stotts, and J. A. Von Arx, "Virtual humans for implantable device safety assessment in MRI: mitigating magnetic resonance imaging hazards for implanted medical devices," *IEEE Pulse*, vol. 8, no. 4, pp. 50–53, 2017.

[39] P. A. Bottomley, A. Kumar, W. A. Edelstein, J. M. Allen, and P. V. Karmarkar, "Designing passive MRI-safe implantable conducting leads with electrodes," *Medical Physics*, vol. 37, no. 7, pp. 3828–3843, 2010.

[40] R. Das and H. Yoo, "RF heating study of a new medical implant lead for 1.5 T, 3 T, and 7 T MRI systems," *IEEE Transactions on Electromagnetic Compatibility*, vol. 59, no. 2, pp. 360–366, 2017.

[41] E. Mattei, E. Lucano, F. Censi, L. M. Angelone, and G. Calcagnini, "High dielectric material in MRI: Numerical assessment of the reduction of the induced local power on implanted cardiac leads," in *Proceedings of the Annual International Conference of the IEEE Engineering in Medicine and Biology Society*, Oct. 2016, pp. 2361–2364.

[42] Z. Yu, X. Xin, and C. M. Collins, "Potential for high-permittivity materials to reduce local SAR at a pacemaker lead tip during MRI of the head with a body transmit coil at 3 T," *Magnetic Resonance in Medicine*, vol. 78, no. 1, pp. 383–

386, 2017.

[43] H. Mosallaei and K. Sarabandi, “A one-layer ultra-thin meta-surface absorber,” in *IEEE Antennas and Propagation Society, AP-S International Symposium (Digest)*, 2005.

[44] M. S. Sarto, C. Caneva, I. M. De Rosa, F. Sarasini, F. Sarto, and A. Tamburrano, “Design and realization of transparent absorbing shields for RF EM fields,” in *IEEE Antennas and Propagation Society, AP-S International Symposium (Digest)*, 2006.

[45] M. S. Sarto, A. Tamburrano, and F. Sarto, “Shielding performances of innovative transparent metals against radio frequency EM fields,” in *IEEE International Symposium on Electromagnetic Compatibility*, 2004.

[46] C. A. Grimes, “EMI shielding characteristics of permalloy multilayer thin films,” in *IEEE Aerospace Applications Conference Proceedings*, 1994.

[47] C. P. Favazza, D. M. King, H. A. Edmonson, J. P. Felmlee, P. J. Rossman, N. J. Hangiandreou, R. E. Watson, and K. R. Gorny, “Use of a radio frequency shield during 1.5 and 3.0 tesla magnetic resonance imaging: experimental evaluation,” *Medical Devices: Evidence and Research*, vol. 7, pp. 363-370, 2014.

[48] F. G. Shellock, J. Begnaud, and D. M. Inman, “Vagus nerve stimulation therapy system : in vitro evaluation of magnetic resonance imaging-related heating and function at 1.5 and 3 Tesla,” *Neuromodulation: Technology at the Neutal Interface*, vol. 9, no. 3, pp. 204–213, 2006.

[49] E. L. Foldes, D. M. Ackermann, N. Bhadra, K. L. Kilgore, and N. Bhadra, “Design, fabrication and evaluation of a conforming circumpolar peripheral nerve

cuff electrode for acute experimental use," *Journal of Neuroscience Methods*, vol. 196, no. 1, pp. 31–37, 2011.

[50] J. Liu, J. Zheng, Q. Zeng, Q. Wang, J. Rondoni, J. Olsen, W. Kainz, and J. Chen, "Investigations on tissue-simulating medium for MRI RF safety assessment for patients with active implantable medical devices," *IEEE Transactions on Electromagnetic Compatibility*, vol. 61, no. 4, pp. 1091–1097, 2019.

[51] T. W. Athey, "A model of the temperature rise in the head due to magnetic resonance imaging procedures," *Magnetic Resonance in Medicine*, vol. 9, no. 2, pp. 177-184, 1989.

[52] P. Nordbeck, F. Fidler, M. T. Friedrich, I. Weiss, M. Warmuth, D. Gensler, V. Herold, W. Geistert, P. M. Jakob, G. Ertl, O. Ritter, M. E. Ladd, W. R. Bauer, and H. H. Quick, "Reducing RF-related heating of cardiac pacemaker leads in MRI : implementation and experimental verification of practical design changes," *Magnetic Resonance In Medicine*, vol. 68, no. 6, pp. 1963–1972, 2012.

[53] Q. X. Yang, J. Wang, J. Wang, C. M. Collins, C. Wang, and M. B. Smith, "Reducing SAR and enhancing cerebral signal-to-noise ratio with high permittivity padding at 3 T," *Magnetic Resonance in Medicine*, vol. 65, no. 2, pp. 358–362, 2011.

[54] B. S. Park, S. S. Rajan, J. W. Guag, and L. M. Angelone, "A novel method to decrease electric field and SAR using an external high dielectric sleeve at 3 T head MRI: numerical and experimental results," *IEEE Transactions on Biomedical Engineering*, vol. 62, no. 4, pp. 1063–1069, 2015.

[55] B. S. Park, B. Mccright, L. M. Angelone, A. Razjouyan, and S. S. Rajan,

"Improvement of electromagnetic field distributions using high dielectric constant (HDC) materials for CTL-spine MRI: numerical simulations and experiments," *IEEE Transactions on Electromagnetic Compatibility*, vol. 59, no. 5, pp. 1382–1389, 2017.

[56] X. Huang, J. Zheng, X. Wu, M. Kono, H. Hozono, W. Kainz, F. Yang, and J. Chen, "MRI heating reduction for external fixation devices using absorption material," *IEEE Transactions on Electromagnetic Compatibility*, vol. 57, no. 4, pp. 635–642, 2015.

[57] P. Nordbeck, F. Fidler, I. Weiss, M. Warmuth, M. T. Friedrich, P. Ehses, W. Geistert, O. Ritter, P. M. Jakob, M. E. Ladd, H. H. Quick, and W. R. Bauer, "Spatial distribution of RF-induced E-fields and implant heating in MRI," *Magnetic Resonance in Medicine*, vol. 60, no. 2, pp. 312–319, 2008.

[58] E. Mattei, G. Gentili, F. Censi, M. Triventi, and G. Calcagnini, "Impact of capped and uncapped abandoned leads on the heating of an MR-conditional pacemaker implant," *Magnetic Resonance in Medicine*, vol. 73, no. 1, pp. 390–400, 2015.

[59] D. A. Langman, I. B. Goldberg, J. Judy, J. Paul Finn, and D. B. Ennis, "The dependence of radiofrequency induced pacemaker lead tip heating on the electrical conductivity of the medium at the lead tip," *Magnetic Resonance in Medicine*, vol. 68, no. 2, pp. 606–613, 2012.

[60] A. C. Özen, T. Lottner, and M. Bock, "Safety of active catheters in MRI: Termination impedance versus RF-induced heating," *Magnetic Resonance in Medicine*, vol. 81, no. 2, pp. 1412–1423, 2019.

[61] J. T. Vaughan, H. P. Hetherington, J. O. Otu, J. W. Pan, and G. M. Pohost, "High

frequency volume coils for clinical NMR imaging and spectroscopy," *Magnetic Resonance in Medicine*, vol. 32, no. 2, pp. 206–218, 1994.

[62] J. T. Vaughan, G. Adriany, M. Garwood, E. Yacoub, T. Duong, L. DelaBarre, P. Andersen, and K. Ugurbil, "Detunable transverse electromagnetic (TEM) volume coil for high-field NMR," *Magnetic Resonance in Medicine*, vol. 47, no. 5. pp. 990–1000, 2002.

[63] J. T. Vaughan and J. R. Griffiths, *RF Coils for MRI*. John Wiley & Sons, 2012.

[64] C. Wang and G. X. Shen, "B1 field, SAR, and SNR comparisons for birdcage, TEM, and microstrip coils at 7T," *Journal of Magnetic Resonance Imaging*, vol. 24, no. 2, pp. 439–443, 2006.

[65] D. T. B. Yeo, Z. Wang, W. Loew, M. W. Vogel, and I. Hancu, "Local specific absorption rate in high-pass birdcage and transverse electromagnetic body coils for multiple human body models in clinical landmark positions at 3T," *Journal of Magnetic Resonance Imaging*, vol. 33, no. 5, pp. 1209–1217, 2011.

[66] S. Pisa, G. Calcagnini, M. Cavagnaro, E. Piuzzi, E. Mattei, and P. Bernardi, "A study of the interaction between implanted pacemakers and the radio-frequency field produced by magnetic resonance imaging apparatus," *IEEE Transactions on Electromagnetic Compatibility*, vol. 50, no. 1, pp. 35–42, 2008.

[67] S. Pisa, P. Bernardi, A. Bicchieri, A. Fabrizi, and E. Piuzzi, "Interaction between MRI RF field and pacemaker holders: a comparison between birdcage and TEM coils in 3 T systems," in *Proceedings of the 5th European Conference on Antennas and Propagation, EUCAP*, 2011, pp. 1942–1945.

[68] Y. Liu, J. Chen, F. G. Shellock, and W. Kainz, "Computational and experimental

studies of an orthopedic implant: MRI-related heating at 1.5-T/64-MHz and 3-T/128-MHz," *Journal of Magnetic Resonance Imaging*, vol. 37, no. 2, pp. 491–497, 2013.